PET data analysis

PET images were realigned to correct for inter-scan head movements by using statistical parametric mapping (SPM 99, Wellcome Department of Cognitive Neurology, London) implemented in Matlab (Mathworks, Sherborn, Mass., USA) [10]. PET images with left eye stimulation were flipped right-to-left so that the stimulated eye could be placed on the right in the PET image. This procedure made it possible to make a direct comparison of the ipsi-lateral or contra-lateral sides to stimulation of the sound eye and the amblyopic eye of each patient.

To evaluate the magnitude of V1 activation, regions of interest were placed on ipsi-lateral and contra-lateral V1. The rCBF response to 6-Hz stimuli and 25-Hz stimuli was measured in these regions.

Group analysis was performed by using SPM99 to estimate the condition effects, voxel by voxel, according to the general linear model. The design matrix included global activity as a confounding covariate; this analysis can therefore be regarded as an ANCOVA [10]. We performed the following three analysis.

First, to investigate the rCBF changes in the primary visual cortex (V1) under each stimulus condition, contrasts of 6 Hz to the sound eye minus rest, 6 Hz to the amblyopic eye minus rest, 25 Hz to the sound eye minus rest, and 25 Hz to the amblyopic eye minus rest were examined.

Second, to compare the differences between ipsi-lateral and contra-lateral stimulation on rCBF in the responses in area V1, 6 Hz to the sound eye minus flipped 6 Hz to the sound eye, flipped 6 Hz to the sound eye minus 6 Hz to the sound eye, 25 Hz to the sound eye minus flipped 25 Hz to the sound eye, and flipped 25 Hz to the sound eye minus 25 Hz to the sound eye were examined.

Third, to test the difference between sound and amblyopic eyes, the contrast of 6 Hz to the sound eye minus 6 Hz to the amblyopic eye, and the contrast of 25 Hz to the sound eye minus 25 Hz to the amblyopic eye were examined.

The first analysis reported as being activated exceeded the $P<0.05$ level of significance ($Z>2.80$, corrected), and regions larger than 100 voxels in cluster size were selected in order to exclude small blobs, which were expected to be emerged by noise. The second and the third analysis were made by masking the image of the V1 according to the small volume correction method [28], because we had formed the hypothesis that a different response would be observed in the V1 with the flicker stimuli of the sound eye and the amblyopic eye. Horton et al. [14] had reported localization and retinotopic organization of the V1 (striate cortex or V1). We made the voxel volume of interest (VVOI) image of a canonical image for an MRI T1-weighted image attached to the SPM99 package. The resulting set of voxel values for each contrast constituted a statistical parametric map of the t statistic SPM (t). The significance of each region was estimated by using distributional approximations from the theory of Gaussian fields [29].

Results

The amplitude of rCBF response of the contra-lateral or ipsi-lateral area V1 to the 6-Hz and 25-Hz stimuli of the sound and amblyopic eye is shown in Fig. 1. The activation

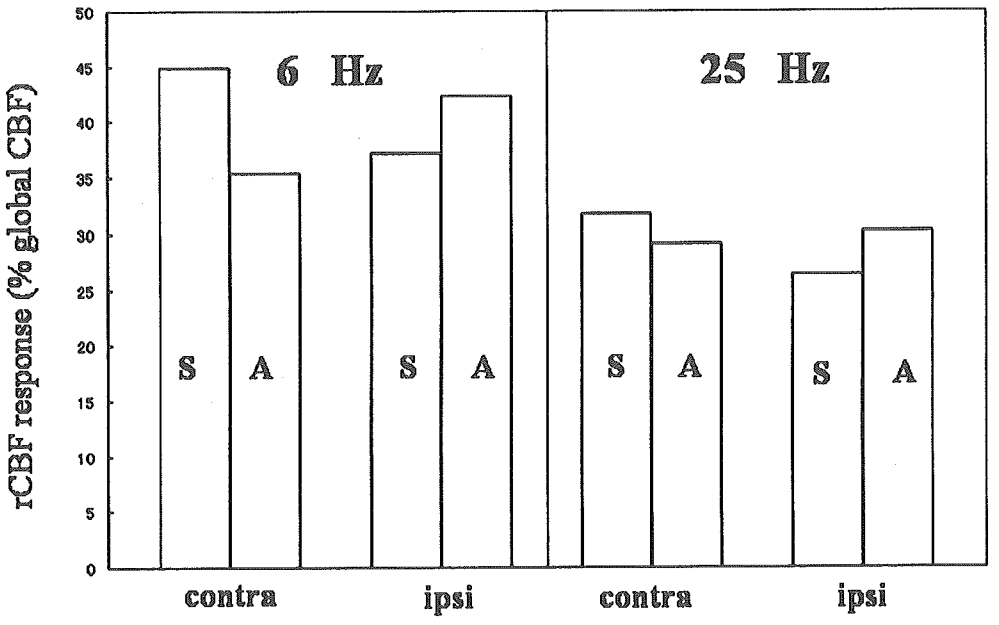

Fig. 1 The mean regional cerebral blood flow (*rCBF*) response of the contra-lateral or ipsi-lateral area V1 to the 6-Hz and 25-Hz stimulation of the sound and amblyopic eye (n=6)

S=sound eye, A=amblyopic eye, contra=contralateral V1 area, ipsi=ipsilateral V1 area

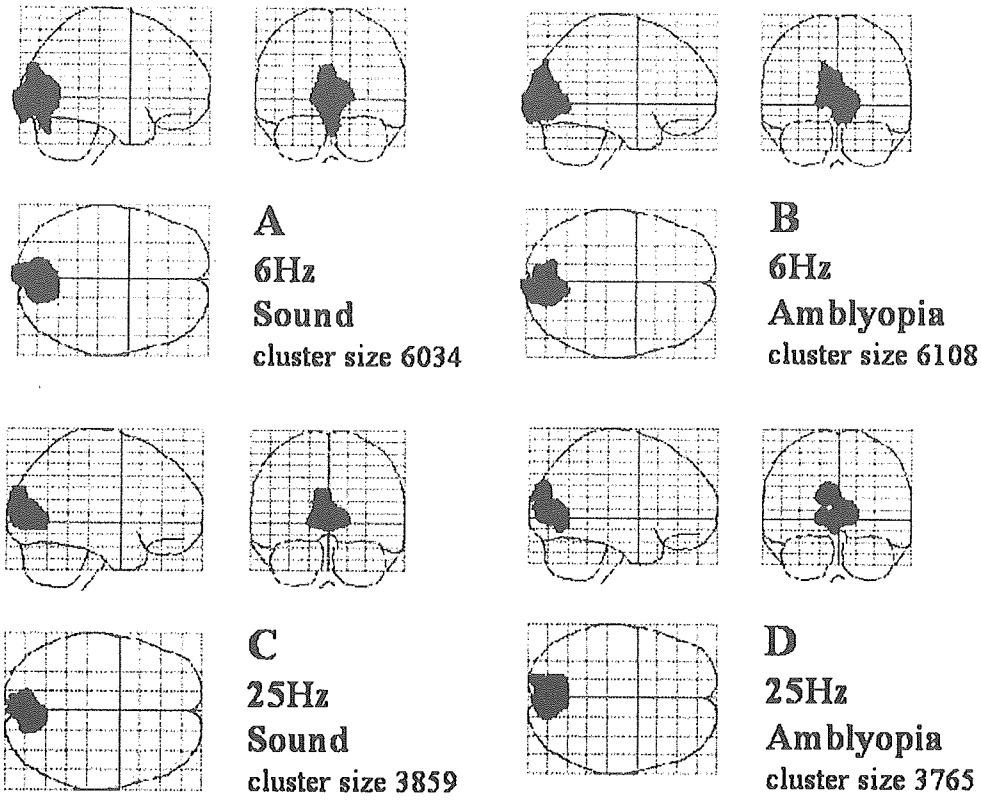

Fig. 2 Statistical map showing that the area V1 is activated bilaterally when the sound and amblyopic eyes are stimulated with 6 Hz and 25 Hz (n=6). Suprathreshold (P<0.05; corrected) areas are displayed on a glass brain. The *gray scale* corresponds to t-value. The *darker* the *gray scale*, the higher the t-value. The cluster size represents the number of suprathreshold voxels. The size of each voxel was 2×2×2 mm^3. **A** 6 Hz to the sound eye minus rest. **B** 6 Hz to the amblyopic eye minus rest. **C** 25 Hz to the sound eye minus rest. **D** 25 Hz to the amblyopic eye minus rest

of contra-lateral V1 by the 6-Hz stimulation of the sound eye was 20% greater than that of the ipsi-lateral V1. The difference tended to be larger in the anisometropic patients (n=3, 36%) compared with the strabismic patients (n=3, 4%). There were no significant correlations between the visual acuity of the amblyopic eye and the rCBF response of the contra- or ipsi-lateral area V1 to the 6-Hz and 25-Hz stimulation (correlation coefficient, r=0.045 for 6 Hz contra, r=0.213 for 6 Hz ipsi, r=0.351 for 25 Hz contra, r=0.447 for 25 Hz ipsi).

The CBF was significantly activated in area V1 bilaterally on 6-Hz and 25-Hz stimulation of the sound eye and amblyopic (Fig. 2; P<0.05, corrected, n=6). All results corresponded to P=0.0001.

The activation of blood flow in the contra-lateral area V1 by the 6-Hz stimulation of the sound eye was significantly greater than that in the ipsi-lateral area V1 (Fig. 3A, P=0.048; Fig. 3B; P=0.046, small volume correction, n=6). At 25-Hz stimulation, the blood flow responses in the

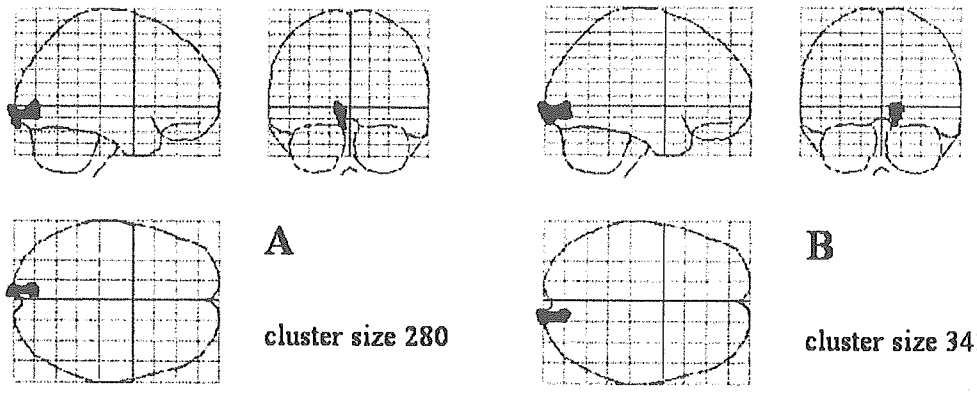

Fig. 3 Statistical map showing that the region of activation of blood flow in the contra-lateral area V1 at 6-Hz stimulation of the sound eye is greater than that following stimulation of the flipped images by group analysis (n=6). Suprathreshold (P<0.05; corrected, small volume correction) areas are displayed on a glass brain. The *gray scale* corresponds to t-value. **A** 6 Hz to the sound eye minus flipped 6 Hz to sound eye. **B** Flipped 6 Hz to the sound eye minus 6 Hz to the sound eye

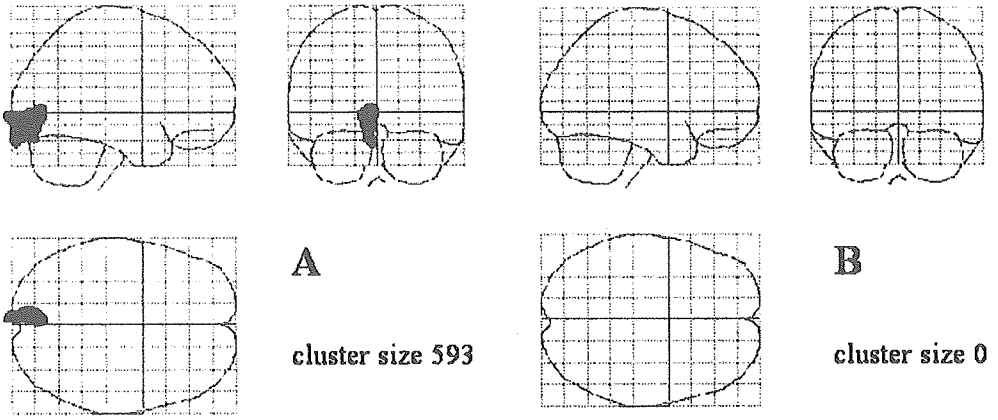

Fig. 4 Statistical map showing that the region of activation of blood flow in the contra-lateral V1 by 6-Hz stimulation of the sound eye is greater than that following stimulation of the amblyopic eye by group analysis (n=6). Suprathreshold (P<0.05; corrected, small volume correction) areas are displayed on a glass brain. The *gray scale* corresponds to t-value. **A** 6 Hz to the sound eye minus 6 Hz to the amblyopic eye. **B** 25 Hz to the sound eye minus 25 Hz to the amblyopic eye

contra-lateral and ipsi-lateral V1 during the stimulation of the sound eye were not significantly different.

The activation of blood flow in the contra-lateral area V1 by 6-Hz stimulation of the sound eye was significantly greater than that following stimulation of the amblyopic eye (Fig. 4A, P=0.042, small volume correction, n=6). However, the activation of blood flow in the ipsi-lateral V1 by the 6-Hz stimulation of the sound was not significantly different from that induced by stimulating the amblyopic eye (Fig. 4A). At 25-Hz stimulation, the blood flow in the contra-lateral and ipsi-lateral V1 of the sound eye and amblyopic eye were not significantly different (Fig. 4B).

Discussion

Parvocellular and magnocellular pathways

The parvocellular and magnocellular pathways differ anatomically, physiologically, and functionally [24]. The low and high temporal frequency stimuli that we used were intended to differentiate the function of these two pathways, i.e., the 6-Hz flicker was expected to activate the parvocellular system and the 25-Hz flicker the magnocellular system.

Evaluation of the parvocellular and magnocellular pathways in strabismic or anisometropic amblyopia by visually evoked potentials has shown that the function of the parvocellular pathway in the amblyopic eye is selectively impaired [9, 25]. Our results confirm these findings and further demonstrate that the impairment is selectively greater for the contra-lateral projections.

Reasons for using flipped PET images to evaluate amblyopic activity

The anterior portion of V1, which serves the temporal visual crescent (60–90° of the visual fields) of the contra-lateral eye, is monocularly innervated. Miki et al. have demonstrated, by fMRI with monocular flicker stimulation [21, 22], that the anterior striate cortex, including not only the monocular area, but also the binocular area, is consistently activated by the contra-lateral eye more than the ipsi-lateral eye. Thus, the comparison of the rCBF between the contra-lateral area V1 during stimulation of the amblyopic eye and the ipsi-lateral area V1 during stimulation of the sound eye will be confounded by the differences of the side of V1. We therefore flipped all PET images with left eye stimulation so that the stimulated eye could be placed on the right side; we could therefore make a direct comparison between the ipsi-lateral or contra-lateral sides of the sound and amblyopic eyes.

Visual cortex activation in amblyopia

From group analysis of PET data, binocular flickering light stimuli induces significant activation in the entire V1 [19, 23]. Our results show that full-field monocular flicker stimulation also effectively activates the entire area V1, which corresponds to the full visual field (Fig. 2).

Functional abnormalities in the visual cortex of amblyopic patients have been demonstrated by using PET [4, 6–8, 17], fMRI [1, 3, 11, 20], and single photon emission computerized tomography (SPECT) [18].

Thus, Choi et al. evaluated the effects of amblyopia on glucose metabolism in the resting state with the eyes open in the occipital lobes by using [^{18}F]-fluorodeoxyglucose PET [4]. They reported that glucose metabolism was decreased in Brodmann area (BA) 17, BAs 18/19, the inferior temporal lobes (BAs 37 and 20), and the superior parietal lobe (BA 7) on both sides of amblyopic patients compared with normal subjects. Although Choi et al. [4] found that the brain function was broadly altered in amblyopic patients, they did not measure the effect of visual stimulation.

Imamura et al. examined the cortical responses evoked by monocular visual stimuli by using $H_2{}^{15}O$ PET [17]. They found that the response to the stimulation of the strabismic amblyopic eye was significantly reduced in the ipsi-lateral BAs 18 and 19. They found no difference in

area V1, presumably because they used checkerboard stimulation, which predominantly activates the association visual cortex. Their study design did not evaluate the effect of laterality comparing the ipsi-lateral side to the amblyopic eye and the contra-lateral side to the sound eye. We have flipped all PET images so that the stimulated eye could be placed on the same side.

Kabasakal et al. used SPECT and reported that the response of the visual cortex to light stimulation of the amblyopic eye was weaker than when the normal eye was stimulated [18]. They did not measure the response in the contra-lateral and ipsi-lateral areas V1 separately. They also combined the results from flicker and checkerboard visual stimuli. Their study design was not intended to differentiate the function of the parvocellular/magnocellular pathways and ipsi-lateral/contra-lateral projections. We have examined the responses between the stimulated and resting state, whereas they compared the responses in only the stimulated state [18].

Activation of area V1 by checkerboard stimulation of different check sizes was compared in anisometropic and strabismic amblyopes by using fMRI by Choi et al. [3]. They observed a significant difference of blood flow activation by 4-Hz and 8-Hz stimuli in anisometropic amblyopes, whereas there was no significant difference at any temporal frequency in area V1 of strabismic amblyopes. They only showed changes between the basal and activated states during calcarine activation. Our study differed from theirs because we compared the blood flow in the ipsi-lateral and contra-lateral sides of the brain in respose to stimulation with respect to the sound and amblyopic eyes. Thus, in our study, the blood flow activation in the contra-lateral area V1 was decreased with 6-Hz stimuli to the amblyopic eye.

Impairment in crossed fibers in amblyopia

In experimental animal models of amblyopia, a reduction has been reported in cell sizes in the lateral geniculate nucleus (LGN) laminae connected with the amblyopic eye [26]. In the LGN of a patient with amblyopia, the decrease was more pronounced in the laminae receiving crossed fibers [27]. Our results showed that the activation of blood flow was also significantly weaker only in the area V1 contra-lateral to the amblyopic eyes, but only with the low temporal frequency stimulation of 6 Hz. However, the activation of blood flow when stimulating the sound eye may have increased. Both the visual cortices and the LGN were affected in previous reports of animal studies [15, 16]. These reasonably suggest that the parvocellular optic nerve fibers, which project contra-laterally from the amblyopic eye, are more affected in amblyopia.

In conclusion, we have shown that the activation of blood flow is lower in the contra-lateral area V1 only when the amblyopic eye is stimulated with a low temporal frequency of 6 Hz. This result supports the hypothesis that the parvocellular optic nerve fibers, which project contra-laterally, are significantly affected in amblyopia.

References

1. Barnes GR, Hess RF, Dumoulin SO, et al (2001) The cortical deficit in humans with strabismic amblyopia. J Physiol (Lond) 533:281–297
2. Campos E (1995) Amblyopia. Surv Ophthalmol 40:23–39
3. Choi MY, Lee KM, Hwang JM, et al (2001) Comparison between anisometropic and strabismic amblyopia using functional magnetic resonance imaging. Br J Ophthalmol 85:1052–1056
4. Choi MY, Lee DS, Hwang JM, et al (2002) Characteristics of glucose metabolism in the visual cortex of amblyopes using positron-emission tomography and statistical parametric mapping. J Pediatr Ophthalmol Strabismus 39:11–19
5. Daw NW (1995) Visual development. Plenum, New York
6. Demer JL (1993) Positron emission tomographic studies of cortical function in human amblyopia. Neurosci Biobehav Rev 17:469–476
7. Demer JL, Noorden GK von, Volkow ND, et al (1988) Imaging of cerebral blood flow and metabolism in amblyopia by positron emission tomography. Am J Ophthalmol 105:337–347
8. Demer JL, Grafton S, Marg E (1997) Positron-emission tomographic study of human amblyopia with use of defined visual stimuli. J AAPOS 1:158–171
9. Demirci H, Gezer A, Sezen F, et al (2002) Evaluation of the functions of the parvocellular and magnocellular pathways in strabismic amblyopia. J Pediatr Ophthalmol Strabismus 39:215–221
10. Friston KJ, Frith CD, Liddle PF, et al (1990) The relationship between global and local changes in PET scans. J Cereb Blood Flow Metab 10:458–466
11. Goodyear BG, Nicolle DA, Humphrey GK, et al (2000) BOLD fMRI response of early visual areas to perceived contrast in human amblyopia. J Neurophysiol 84:1907–1913
12. Grigg J, Thomas R, Billson F (1996) Neuronal basis of amblyopia: a review. Ind J Ophthalmol 44:69–76
13. Herscovitch P, Raichle ME, Kilbourn MR, et al (1987) Positron emission tomographic measurement of cerebral blood flow and permeability-surface area product of water using [^{15}O]water and [^{11}C]butanol. J Cereb Blood Flow Metab 7:527–542
14. Horton JC, Hoyt WF (1991) The representation of the visual field in human striate cortex. A revision of the classic Holmes map. Arch Ophthalmol 6:816–824

15. Hubel DH, Wiesel TN (1970) The period of susceptibility to the physiological effects of unilateral eye closure in kittens. J Physiol (Lond) 206:419–436
16. Hubel DH, Wiesel TN, LeVay S (1977) Plasticity of ocular dominance columns in monkey striate cortex. Philos Trans R Soc Lond Biol 278:377–409
17. Imamura K, Richter H, Fischer H, et al (1997) Reduced activity in the extrastriate visual cortex of individuals with strabismic amblyopia. Neurosci Lett 225:173–176
18. Kabasakal L, Devranoglu K, Arslan O, et al (1995) Brain SPECT evaluation of the visual cortex in amblyopia. J Nucl Med 36:1170–1174
19. Kawasaki T, Kiyosawa M, Ishii K, et al (1998) Regional cerebral blood flow response to visual stimulation measured quantitatively with PET. Neuro-Ophthalmology 20:79–89
20. Lee KM, Lee SH, Kim NY, et al (2001) Binocularity and spatial frequency dependence of calcarine activation in two types of amblyopia. Neurosci Res 40:147–153
21. Miki A, Liu GT, Raz J, et al (2000) Contralateral monocular dominance in anterior visual cortex confirmed by functional magnetic resonance imaging. Am J Ophthalmol 130:821–824
22. Miki A, Liu GT, Englander SA, et al (2001) Functional magnetic resonance imaging of eye dominance at 4 Tesla. Ophthalmic Res 33:276–282
23. Noorden GK von, Middleditch PR (1975) Histology of the monkey lateral geniculate nucleus after unilateral lid closure and experimental strabismus: further observations. Invest Ophthalmol 14:674–683
24. Noorden GK von, Crawford ML, Levacy RA (1983) The lateral geniculate nucleus in human anisometropic amblyopia. Invest Ophthalmol Vis Sci 24:788–790
25. Mizoguchi S, Suzuki Y, Kiyosawa M, et al (2003) Detection of visual activation of lateral geniculate nucleus by positron emission tomography. Graefes Arch Clin Exp Ophthalmol 241:8–12
26. Schiller PH, Logothetis NK (1990) The color-opponent and broad-band channels of the primate visual system. Trends Neurosci 13:392–398
27. Shan Y, Moster ML, Roemer RA, et al (2000) Abnormal function of the parvocellular visual system in anisometropic amblyopia. J Pediatr Ophthalmol Strabismus 37:73–78
28. Worsley KJ, Marrett S, Neelin P, et al (1996) A unified statistical approach for determining significant signals in images of cerebral activation. Hum Brain Mapp 4:58–73
29. Worsley KJ, Andermann M, Koulis T, et al (1999) Detecting changes in nonisotropic images. Hum Brain Mapp 8:98–101

Extraction of a Plasma Time-Activity Curve From Dynamic Brain PET Images Based on Independent Component Analysis

Mika Naganawa, *Member, IEEE*, Yuichi Kimura*, *Member, IEEE*, Kenji Ishii, Keiichi Oda, Kiichi Ishiwata, and Ayumu Matani, *Member, IEEE*

***Abstract*—A compartment model has been used for kinetic analysis of dynamic positron emission tomography (PET) data [e.g., 2-deoxy-2-^{18}F-fluoro-D-glucose (FDG)]. The input function of the model [the plasma time-activity curve (pTAC)] was obtained by serial arterial blood sampling. It is of clinical interest to develop a method for PET studies that estimates the pTAC without needing serial arterial blood sampling. For this purpose, we propose a new method to extract the pTAC from the dynamic brain PET images using a modified independent component analysis [extraction of the pTAC using independent component analysis (EPICA). Source codes of EPICA are freely available at http://www5f.biglobe.ne.jp/~ukimura/Software/top.html]. EPICA performs the appropriate preprocessing and independent component analysis (ICA) using an objective function that takes the various properties of the pTAC into account. After validation of EPICA by computer simulation, EPICA was applied to human brain FDG-PET studies. The results imply that the EPICA-estimated pTAC was similar to the actual measured pTAC, and that the estimated blood volume image was highly correlated with the blood volume image measured using ^{15}O-CO inhalation. These results demonstrated that EPICA is useful for extracting the pTAC from dynamic PET images without the necessity of serial arterial blood sampling.**

***Index Terms*—Compartment model, independent component analysis, plasma time-activity curve extraction, positron emission tomography.**

I. Introduction

In nuclear medicine, positron emission tomography (PET) can yield quantitative information on the spatial distribution of administered radiopharmaceuticals. Recently, much interest has been paid to the analysis of time sequences of the radioactivity in target tissues, which is known as a dynamic PET study, because analysis can produce useful information about various physiological and biological processes in living tissues. The processes related to the radiopharmaceuticals are expressed by an underlying model, which is known as the compartment model. For example, the behavior of 2-deoxy-2-^{18}F-fluoro-D-glucose (FDG) can be described as follows [1], [2]:

$$\begin{aligned} c_{\mathrm{i}}(t) &= (1-V_{\mathrm{B}})c_{\mathrm{t}}(t) + V_{\mathrm{B}}c_{\mathrm{p}}(t) \\ &= (1-V_{\mathrm{B}})\int_0^t h(t-\tau;\mathbf{k})c_{\mathrm{p}}(\tau)\mathrm{d}\tau + V_{\mathrm{B}}c_{\mathrm{p}}(t) \\ \mathbf{k} &= [K_1, k_2, k_3, k_4]^{\mathrm{T}} \\ h(t;\mathbf{k}) &= \frac{K_1}{k_2+k_3}[k_3 + k_2\exp\{-(k_2+k_3)t\}], \quad k_4 = 0. \end{aligned} \tag{1}$$

In (1), $c_{\mathrm{t}}(t)$ is the concentration of FDG in the tissue at time t and is called the tissue time-activity curve (tTAC). The function $c_{\mathrm{p}}(t)$ is called the plasma time-activity curve (pTAC) and is the concentration of FDG in the plasma. $c_{\mathrm{i}}(t)$ is the total concentration of FDG, and V_{B} is the blood volume. The tissue impulse response function is denoted by $h(t;\mathbf{k})$, and $\mathbf{k}$ is a parameter vector that describes the rate of transfer of the tracer. Note that k_4 is assumed to be zero. The pTAC and tTAC can be considered as the input and output functions of the compartment model, respectively. The pTAC values are usually measured by serial blood sampling using a catheter inserted in the brachial artery. However, insertion of the catheter is uncomfortable and is sometimes painful for patients. It is also a time-consuming protocol for a daily clinical scan. It is therefore of clinical interest to develop a method for estimating the pTAC without the need for serial arterial blood sampling.

The factor analysis [3], [4] has been proposed to moderate or eliminate serial arterial blood sampling. Factor analysis approach estimates the pTAC and the blood volume from dynamic images; two methods have been proposed to estimate the pTAC from actual dynamic cardiac PET images: factor analysis of dynamic structures (FADS) [3] and independent component analysis (ICA) [4]. However, a FADS estimation with a nonnegativity constraint has nonunique solutions [5] and therefore requires additional anatomical assumptions to overcome the nonuniqueness. It is difficult to make effective assumptions, because the vascular structure depends on the anatomical situation. On the other hand, ICA seems to be an attractive approach, because it can extract pTAC-related information without any anatomical assumptions. To apply ICA to dynamic PET images correctly, a well-designed preprocessing

Manuscript received September 11, 2003; revised May 25, 2004. This work was supported in part by the Japan Society for the Promotion of Science under the Grant-in-Aid for Scientific Research 16591243 in 2004 and 2005. *Asterisk indicates corresponding author.*

M. Naganawa is with the Department of Information Processing, Graduate School of Information Science, Nara Institute of Science and Technology, Nara 630-0192, Japan.

*Y. Kimura is with Positron Medical Center, Tokyo, Metropolitan Institute of Gerontology, 1-1, Naka, Itabashi, Tokyo 173-0022, Japan (e-mail: ukimura@ieee.org).

K. Ishii, K. Oda, and K. Ishiwata are with Positron Medical Center, Tokyo Metropolitan Institute of Gerontology, Tokyo 173-0022, Japan

A. Matani is with the Department of Complexity Science and Engineering, Graduate School of Frontier Sciences, University of Tokyo, Tokyo 173-0022, Japan.

Digital Object Identifier 10.1109/TBME.2004.840193

and the definition of an objective function to optimize pTAC extraction are necessary. To address these problems, this paper proposes a new method [extraction of the pTAC using independent component analysis (EPICA)] to extract the pTAC from dynamic FDG brain PET images using ICA with appropriate preprocessing and objective function.

II. Theory

Our proposed method, EPICA, is based on FastICA, proposed by Hyvärinen [6]. The theory of FastICA is outlined in Section II-A. Some problems arising from applying FastICA to dynamic PET images are presented in Section II-B. In Sections II-C and II.D, a method for overcoming the problems is proposed. The steps taken in EPICA are summarized in Section II-E.

A. FastICA

Consider a zero-mean, N-dimensional random vector, $\mathbf{s}$, whose elements are assumed to be mutually statistically independent [independent components (ICs)] as

$$\mathbf{s} = [s_1, \ldots, s_N]^{\mathrm{T}}, \quad \mathrm{E}\{s_i\} = 0 \quad (i = 1, \ldots, N).$$

The expectation of s_i is denoted by $\mathrm{E}\{s_i\}$. The ICs are unknown, but linear combinations of the ICs $\mathbf{x} = [x_1, \ldots, x_F]^{\mathrm{T}}$ can be observed (where $\mathbf{x}$ is the F-dimensional random vector). The ICA linear model can be written in the form

$$\mathbf{x} = \mathbf{M}\mathbf{s} \tag{2}$$

where $\mathbf{M}$ is an F-by-N mixing matrix whose elements are unknown mixing coefficients. The goal of ICA is to estimate the original ICs, $\mathbf{s}$, from a given $\mathbf{x}$.

FastICA is a method for IC estimation using an iterative algorithm [6] to maximize an objective function that measures independence in the given data $\mathbf{x}$. In the FastICA algorithm, the first step is a whitening of the given data $\mathbf{x}$. The whitening makes the components uncorrelated from each other and their variances equal unity, and it is performed by multiplying by a whitening matrix, $\mathbf{W}$. The whitened vector, $\mathbf{x}_{\mathrm{w}}$, is represented as

$$\mathbf{x}_{\mathrm{w}} = \mathbf{B}\mathbf{s}, \quad \mathbf{B} \equiv \mathbf{W}\mathbf{M}.$$

The matrix, $\mathbf{B}$, is an orthogonal matrix [7], and therefore ICs are estimated as $\mathbf{s} = \mathbf{B}^{\mathrm{T}}\mathbf{x}_{\mathrm{w}}$. See [6] for the details on whitening. The ith iteration of an optimization algorithm to maximize an objective function, G, is [8]

$$\begin{aligned} \mathbf{b}_i^* &= \mathrm{E}\left\{\mathbf{x}_{\mathrm{w}} g\left(\mathbf{b}_{i-1}^{\mathrm{T}}\mathbf{x}_{\mathrm{w}}\right)\right\} - \mathrm{E}\left\{g'\left(\mathbf{b}_{i-1}^{\mathrm{T}}\mathbf{x}_{\mathrm{w}}\right)\right\}\mathbf{b}_{i-1}, \\ \mathbf{b}_i &= \mathbf{b}_i^*/\|\mathbf{b}_i^*\| \end{aligned} \tag{3}$$

where $\mathbf{b}$ is a column vector of the matrix $\mathbf{B}$, $\mathbf{b}_{i-1}$ is an estimate at the $(i-1)$th iteration, and $g(\cdot)$ is a derivative of the objective function G. The initial vector, $\mathbf{b}_0$, is given as a random vector with unit norm. There are two approaches to estimate several ICs in FastICA, the deflation approach and the symmetric approach. The deflation approach estimates ICs one by one, and the symmetric approach estimates all ICs in parallel. The deflation approach is more desirable in the case where a specific IC is to be estimated [9]. Our proposed method, EPICA, adopts the deflation approach.

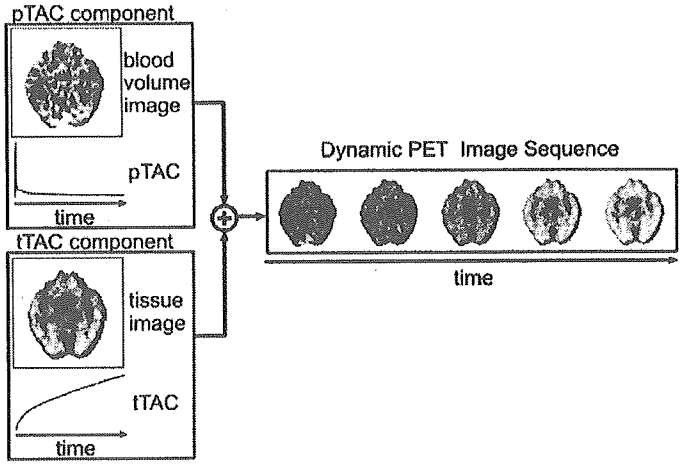

Fig. 1. Illustration of the linear dynamic brain PET model. The dynamic PET images are derived from sequential measurements of the radioactivity after radiopharmaceutical administration. This illustration originated from FDG, which is irreversible and tends to accumulate in brain tissues. The image sequence was assumed to be a sum of the pTAC and tTAC components. Each component consists of a time course and a contribution ratio to the voxels (the blood volume image and the tissue image). The blood volume image shows the spatial distribution of the blood vessels in the target tissue. The aim of the EPICA technique is to estimate the time courses and the blood volume image and tissue image using the measured dynamic PET image sequence.

B. Application of FastICA to Dynamic PET Images

The mixing process in (2) and independence are considered in relation to dynamic PET data as given below. The value of the qth voxel of the PET image at time, t, is described by

$$x(q,t) = s_{\mathrm{p}}(q)c_{\mathrm{p}}(t) + s_{\mathrm{t}}(q)c_{\mathrm{t}}(t) \quad (q = 1, \ldots, Q)$$

where Q is the total number of voxels, $s_{\mathrm{p}}(q)$ is determined by the ratio of the tissue blood volume to the qth voxel, $s_{\mathrm{t}}(q)$ is determined by the scale of the tTAC values and the ratio of the brain tissue to the qth voxel, and $c_{\mathrm{p}}(t)$ and $c_{\mathrm{t}}(t)$ are the pTAC and the tTAC, respectively. An illustration of the linear dynamic PET model is shown in Fig. 1. Note that the pTAC is common in the brain; however, the scale of the tTAC varies by voxels. Therefore, $s_{\mathrm{p}}(t)$ is simply the ratio of blood volume to voxel volume, and $s_{\mathrm{t}}(t)$ is determined by the ratio of tissue volume to voxel volume and the scale of the tTAC in the voxel. The history of the concentration of FDG at the qth voxel, $\mathbf{x}(q)$, can be represented by

$$\mathbf{x}(q) = s_{\mathrm{p}}(q)\mathbf{c}_{\mathrm{p}} + s_{\mathrm{t}}(q)\mathbf{c}_{\mathrm{t}} \tag{4}$$

where $\mathbf{x}(q)$, $\mathbf{c}_{\mathrm{p}}$, and $\mathbf{c}_{\mathrm{t}}$ are column vectors. In matrix notation, (4) can be represented as

$$\mathbf{X} = [\mathbf{c}_{\mathrm{p}} \quad \mathbf{c}_{\mathrm{t}}][\mathbf{s}_{\mathrm{p}} \quad \mathbf{s}_{\mathrm{t}}]^{\mathrm{T}} = \mathbf{C}\mathbf{S}. \tag{5}$$

Here, $\mathbf{X}$ is the dynamic PET image matrix, and in this paper, $\mathbf{s}_{\mathrm{p}}$ and $\mathbf{s}_{\mathrm{t}}$ are the blood volume image and the tissue image, respectively.

In the ICA model, $\mathbf{C}$ and $\mathbf{S}$ in (5) are regarded as the mixing matrix and the source matrix, respectively. The dynamic PET image sequence is assumed to be a linear combination of spatially independent images, namely the blood volume image and the tissue image. The pTAC is a column of the mixing matrix $\mathbf{C}$. Note that independence is not assumed in time-activity curves (TACs), but in their spatial distributions. If FastICA is applied to

the measured dynamic PET images, the pTAC is not estimated correctly. This is because the objective function is not appropriate to estimate the pTAC, and the probability distributions of the voxel values in the blood volume image and the tissue image, also known as image priors (the probability distributions that generate the voxel values), are not known in advance. Therefore, modifications to FastICA are required to estimate the pTAC exactly. The performance of the objective functions are described in Section III.A. The modifications consist of preprocessing the measured dynamic PET images and the design of an appropriate objective function for FastICA. The details of these modifications are described in Section II-C.

C. Preprocessing

The preprocessing of the measured PET images consists of two steps: appending negative images and enhancing the difference of the statistical properties of the blood volume and tissue images.

1) Negative Images: ICA assumes a zero mean source signal; therefore, the mean values of the blood volume image and the tissue image are required to be zero. The zero mean data were generated by concatenating each data vector, $\mathbf{x}(q)$, with its negative, $-\mathbf{x}(q)$. This negative image appending is formed as

$$\begin{aligned}\mathbf{X}_{\mathrm{N}} = [\mathbf{X}, -\mathbf{X}] &= \mathbf{c}_{\mathrm{p}}\left[\mathbf{s}_{\mathrm{p}}^{\mathrm{T}}, -\mathbf{s}_{\mathrm{p}}^{\mathrm{T}}\right] + \mathbf{c}_{\mathrm{t}}\left[\mathbf{s}_{\mathrm{t}}^{\mathrm{T}}, -\mathbf{s}_{\mathrm{t}}^{\mathrm{T}}\right] \\ &= \mathbf{c}_{\mathrm{p}}\mathbf{s}_{\mathrm{pN}}^{\mathrm{T}} + \mathbf{c}_{\mathrm{t}}\mathbf{s}_{\mathrm{tN}}^{\mathrm{T}}.\end{aligned}$$

Note that this appending procedure is used here for the purpose of explanation only and will never actually be performed. The appended images have a perfectly symmetrical distribution, and therefore the actual appending procedure makes no difference to the results, but it enlarges the calculation cost.

2) Difference-Enhanced Images: FastICA estimates ICs using an objective function that evaluates the non-Gaussianity of the components. The probability distributions of the ICs are non-Gaussian, and each has different statistical properties. The distributions of the blood volume image, $\mathbf{s}_{\mathrm{pN}}$, and the tissue image, $\mathbf{s}_{\mathrm{tN}}$, are not available as *a priori* information, because these distributions depend on the subjects' physiological condition. To estimate pTAC using FastICA, a transformation is required that enhances the difference of the probability distributions between two images, ($\mathbf{s}_{\mathrm{pN}}$ and $\mathbf{s}_{\mathrm{tN}}$). EPICA transforms the dynamic PET data via standardization using the time integral of the absolute value of each voxel for the enhancement. The time integral is calculated using the trapezoidal integration method.

The effect of enhancement is explained using two anatomically reasonable constraints, as follows:

- A1) The ratio of blood volume to whole brain volume is very small (typically 2%–4% [1], [10], [11]).
- A2) There are few voxels, typically 1%–2% of total voxels, whose blood volume ratios are more than 30%.

The blood volume in each voxel represents the ratio of blood volume to the voxel's volume and can be measured using ^{15}O-CO inhalation [12].

The properties of the enhanced blood volume and tissue images are as follows. The time integral of the qth voxel's TAC, $A_{\mathrm{x}}(q)$, is described by

$$A_{\mathrm{x}}(q) = \left|\int_0^{T_{\mathrm{E}}} x(q,t)\mathrm{d}t\right| = A_{\mathrm{p}}s_{\mathrm{p}}(q) + A_{\mathrm{t}}s_{\mathrm{t}}(q)$$

where T_{E} denotes the time of the final frame, and A_{p} and A_{t} are the pTAC and tTAC time integrals, respectively. The enhanced TAC, $x_{\mathrm{E}}(q,t)$, is represented by

$$x_{\mathrm{E}}(q,t) = \frac{x(q,t)}{A_{\mathrm{x}}(q)} = c_{\mathrm{pE}}(t)s_{\mathrm{pE}}(q) + c_{\mathrm{tE}}(t)s_{\mathrm{tE}}(q)$$

where

$$\int_0^{T_{\mathrm{E}}} c_{\mathrm{pE}}(t)\mathrm{d}t = 1, \quad \int_0^{T_{\mathrm{E}}} c_{\mathrm{tE}}(t)\mathrm{d}t = 1.$$

The values of $s_{\mathrm{pE}}(q)$ and $s_{\mathrm{tE}}(q)$ are called the enhanced blood volume and tissue images, respectively. We divided the properties of these images into two cases. In the first case, the tTAC time integral is much larger than the pTAC time integral, $A_{\mathrm{x}} \simeq s_{\mathrm{t}}(q)A_{\mathrm{t}}$. The voxel values of the enhanced blood volume image are mostly distributed around $0, 0 \leq |s_{\mathrm{pE}}| \ll 1$, whereas those of the enhanced tissue image are around 1 or $-1, |s_{\mathrm{tE}}| \simeq 1$. As described above, with two constraints (A1 and A2), almost all voxels belong to the first case, because there are few voxels where the pTAC time integral dominates. In the second case, the pTAC time integral is much larger than the tTAC time integral, $A_{\mathrm{x}} \simeq s_{\mathrm{p}}(q)A_{\mathrm{p}}$. In this case, the two enhanced images are $0 \leq |s_{\mathrm{tE}}| \ll 1$ and $|s_{\mathrm{pE}}| \simeq 1$. The effect of standardization is summarized as follows: the time integral of the pTAC is much smaller than that of the tTAC. Note that the time integral of the tTAC in each voxel depends on both the ratio of tissue volume to voxel volume and the scale ($\gg$1) of the tTAC. In addition, the blood volume is very small in almost all voxels. Therefore, the time integrals of TACs of almost all voxels are approximately equal to the time integral of tTAC. Standardization forces the voxel values of the tTAC image to 1 or -1, and those of the pTAC image to near zero. Consequently, the two enhanced blood volume and tissue images will have the following properties.

- P1) The distribution of the enhanced blood volume image has a sharper peak and longer tails than the Gaussian distribution. The long tail distribution has tails that decay more slowly than those of the Gaussian distribution [13]. The voxel values of the image vary from approximately -1 to 1.
- P2) The voxel values of the enhanced tissue image are approximately divided into 1 and -1.

Fig. 2 shows the transformation of the blood volume image and the tissue image of the simulated images by the enhancement. The method for generating the simulated PET data is presented in Section III-A.

The objective function of FastICA is designed to take the properties of the two images into account.

D. Design of the Objective Function

The whitened blood volume image has long tails whose absolute values are much greater than one as described in Sec-

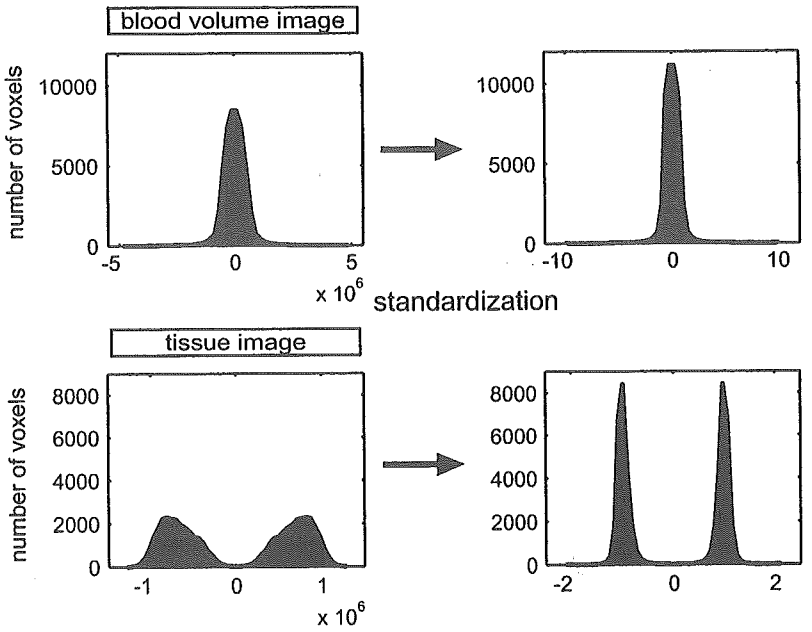

Fig. 2. The histograms of voxel values of the blood volume and tissue images generated from the simulated images. Standardization enhances the difference between the distributions for the measured blood volume and tissue images. The distribution of the blood volume image was transformed into the distribution with a sharper peak and longer tails, and the voxel values of the tissue image were concentrated to 1 or -1.

tion II-C2. On the other hand, the voxel values of the whitened tissue image are near 1 or -1, the same as for the tissue image before whitening. In general, the whitened blood volume image has long tails and the whitened tissue image has short tails. Therefore, the objective function needs to be sensitive to distributions having long tails in order to extract the pTAC from the whitened PET data. In choosing a fast-growing objective function, G (for example, $G(u) = u^6$, where u is the whitened PET data), the blood volume image can be estimated by maximizing the objective function. However, under the condition that the variance is equal to one, the objective function is maximized not by the true blood volume image, but by the estimated image having long tails that include negative values, as shown in Fig. 3. To prevent the voxel values from being concentrated near zero, a penalty term is added to the objective function. The objective function used for the pTAC extraction was

$$G(u) = u^6 - \frac{\lambda}{m} \exp\left(-\frac{|u|}{m}\right) \tag{6}$$

where λ and m are positive parameters ($10 < \lambda < 100$ and $0.1 < m < 0.5$). The first term grows fast so that it is effective in detecting the long tails, while the second term keeps the voxel values from over-concentrating near zero.

EPICA adopts the fast fixed-point algorithm the convergence of which is cubic. This algorithm does not always maximize the objective function. The proposed objective function of EPICA is designed to extract the pTAC by maximizing the objective function, but EPICA does not guarantee the extraction of the pTAC when the objective function is minimized. Note that a deflation approach has the drawback that the errors in the first estimation accumulate in the subsequent estimations [9]. Because it is important to accurately estimate the pTAC in this study, the pTAC needs to be estimated as the "first" IC, by "maximizing" the objective function. However, two solutions that maximize

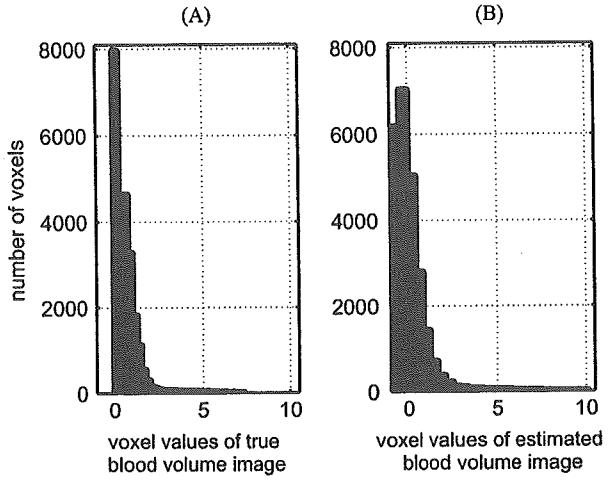

Fig. 3. Histograms of voxel values of (A) the true blood volume image, and (B) the estimated blood volume image using an objective function, $G(u) = u^6$, from the simulated PET images. The blood volume images derived only from the original images are shown. The method of generating the simulated PET data is presented in Section III-A. The tail of the estimated blood volume image is longer than that of the true blood volume image, and the estimated blood volume image has negative values. A term preventing the voxel values from being concentrated near zero is required for the objective function, $G(u)$.

or minimize the objective function are found by EPICA. The shape of the first estimated TAC is helpful in deriving the unique pTAC estimate because pTAC and tTAC have different shapes from each other. If the shape of the first estimated TAC is different from the typical shape of a pTAC by visual inspection, the EPICA technique is rerun with another random initial vector until the first estimated TAC has a pTAC-like shape. The initial vector is generated from a uniform random distribution. Usually, the estimate of pTAC is obtained within one or two runs of the proposed algorithm. Practically, the nonuniqueness in EPICA does not affect the estimation of the pTAC.

E. Procedure of EPICA

The EPICA procedure is summarized below.

Step 1) Append negative images to achieve the zero-mean source signal that the ICA algorithm requires.

Step 2) Standardize each voxel's TAC by the time integral to emphasize pTAC-related information.

Step 3) To obtain a stable estimation, reduce the dimension of the dynamic PET image sequence to two using principal component analysis (PCA).

Step 4) Apply FastICA (a deflation approach) to the dynamic PET images.

Step 5) Adjust the scale of the estimated pTAC values using one-point arterial blood sampling data.

In Step 3), eigenvalues of $\mathrm{E}\{\mathbf{x}\mathbf{x}^{\mathrm{T}}\}$ are calculated and $\mathbf{X}$ is projected onto the plane spanned by the two eigenvectors that have the largest eigenvalues [14]. This dimension reduction by PCA often has the effect of reducing noise. Note that a random vector having unit norm is taken as the initial estimation of ICA in Step 4). The expectations in (3) can be calculated exactly, because $\mathbf{x}_{\mathrm{w}}$ is whitened, measured dynamic data, and g is a defined function, given in Section II-D. Because ICA cannot determine the scale, sign, and ordering of the estimated ICs, Step 5) is required to derive these quantities.

III. Experiments

Computer-simulated dynamic PET and human FDG-PET images were used to evaluate the performance of EPICA.

A. Computer Simulations

Simulated PET images were generated based on three clinical data sets. Dynamic FDG-PET images and arterial plasma samples were measured simultaneously, and a blood volume image was also acquired from ^{15}O-CO inhalation in a successive scan. The simulated PET images contained seven slices, and each slice consisted of 128 × 128 voxels. The frame arrangement was determined based on the actual arterial plasma sample timing used in the PET Center of the Tokyo Metropolitan Institute of Gerontology (TMIG). The timing of the arterial sampling is shown in Table I.

A total of 24 arterial samplings were performed. The frame arrangement of the dynamic PET images was based on the arterial plasma sample timing: 0.3 s, 10.5 (= 10.8 − 0.3) s, 8 (= 18.8−10.8) s, etc. The simulated PET images were calculated as the sum of three components: a pTAC, a tTAC, and a noise component, which are denoted by $C_{\mathrm{pTAC}}(q,t)$, $C_{\mathrm{tTAC}}(q,t)$, and $C_{\mathrm{noise}}(q,t)$, respectively.

The pTAC component was calculated from the measured pTAC and blood volume using the following equation:

$$C_{\mathrm{pTAC}}(q,t) = V_{\mathrm{B}}(q)c_{\mathrm{p}}(t)$$

where $V_{\mathrm{B}}(q)$ represents the blood volume measured by PET at the qth voxel, and $c_{\mathrm{p}}(t)$ is the measured pTAC using arterial blood sampling. The true pTAC and true blood volume image correspond to $c_{\mathrm{p}}(t)$ and $V_{\mathrm{B}}(q)$, respectively.

The calculation of the tTAC component consisted of the following four steps.

TABLE I
Timing for Arterial Sampling

number	time (sec)	number	time (sec)
1	0.3	13	87.3
2	10.8	14	94.3
3	18.8	15	117.3
4	25.3	16	170.3
5	32.3	17	299.8
6	38.8	18	408.8
7	46.3	19	575.3
8	51.8	20	894.3
9	58.3	21	1178.3
10	65.8	22	1761.3
11	72.3	23	2425.3
12	79.8	24	3741.8

Step 1) Apply a 5-by-5 averaging filter to the dynamic PET images. Each voxel value is replaced by the averaged value in a 5-by-5 block of neighbors.

Step 2) Estimate the kinetic microparameters, (K_1, k_2, k_3), of each voxel using an ordinal nonlinear least squares algorithm.

Step 3) Calculate the noise-free tTACs, $c_{\mathrm{t}}(q,t)$, by substituting the measured pTAC values and the estimated parameters into (1).

Step 4) Multiply the tTAC component by the ratio of the brain tissue volume to each voxel volume

$$C_{\mathrm{tTAC}}(q,t) = (1 - V_{\mathrm{B}}(q))c_{\mathrm{t}}(q,t).$$

The noise-free TAC at the qth voxel, $C_{\mathrm{T}}(q,t)$, was the sum of the pTAC and the tTAC components.

The noise component was assumed to be Gaussian, with zero mean and variance, $C_{\mathrm{T}}(q,t)/\Delta t$, satisfying

$$C_{\mathrm{noise}}(q,t) \sim N\left(0, \alpha\frac{C_{\mathrm{T}}(q,t)}{\Delta t}\right) \tag{7}$$

where α determines the noise level, and Δt is the width of a frame. The noise level was set to 30 to be comparable to the clinical case.

Ten simulated data items were generated, and then EPICA was applied. The difference between the data items is the noise component. The noise was randomly generated according to (7). The stopping criterion was that the norm of the difference between two successive columns of the separating matrix be less than 0.0001 ($\|\mathbf{b}_i^* - \mathbf{b}_i\| < 0.0001$). The stepwidth is not required because FastICA is a fixed-point algorithm as shown in (6). The scale of the estimated pTAC values was adjusted using the peak of the true pTAC values. Fig. 4 shows the estimated pTAC using EPICA compared with the true pTAC. The shape of the estimated pTAC using EPICA is similar to the true pTAC form. This figure presents an example of 10 results, and the results were consistent over all 10 simulated PET images. If the parameters consisting of the objective function, λ and m, were changed, very similar results were obtained. An empirical value of $\lambda = 50$, and $m = 0.3$ was used in this simulation.

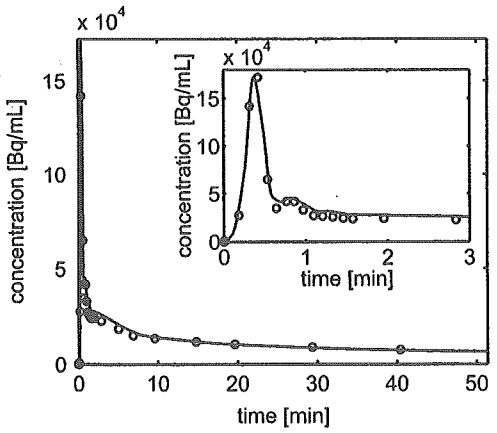

Fig. 4. Estimation results from the simulated PET images. pTAC-like estimate by EPICA (solid line) and the true pTAC values (open circles). The estimated pTAC values were scaled so that the peak value corresponded to the true pTAC values. A magnified view of the first section of the PET data is shown in the inset. The parameters of the objective function in (6) were $\lambda = 50$ and $m = 0.3$. The noise level of the simulated PET data was similar to the clinical noise level. A total of 24 974 voxels were used to extract the pTAC.

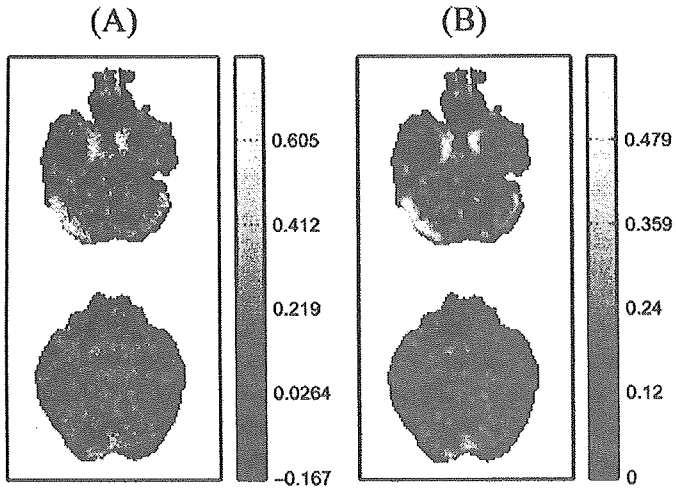

Fig. 5. (A) The blood volume image estimated from the simulated FDG-PET images using EPICA, and (B) the true blood volume image measured by PET using ^{15}O-CO inhalation. Blood volume image (B) was the image used to calculate the pTAC component of the simulated PET data. The noise level of the simulated PET data was similar to the clinical noise level. The parameters of the objective function in (6) were $\lambda = 50$ and $m = 0.3$.

For validation of EPICA, the estimated blood volume image from EPICA and the true blood volume image were compared, and the correlation coefficient of these two images was calculated. Fig. 5 shows the estimated blood volume image from EPICA and the true blood volume image. Although the estimated blood volume image includes some negative voxels, it is still very similar to the true blood volume image. Fig. 6 shows the relationship of the voxel values between the two blood volume images, which show a good correlation ($y = 1.09x - 7.06 \times 10^{-2}$) with a correlation coefficient of 0.83. The calculation time was approximately 10 s for the 128-by-128 scan with 30 slices of data using a PC with an Intel Pentium III processor, a clock speed of 866 MHz, and 256 MB of memory. The number of iterations was between 10 and 20.

To compare EPICA with the original general purpose FastICA, the estimation of the pTACs and the blood volume images

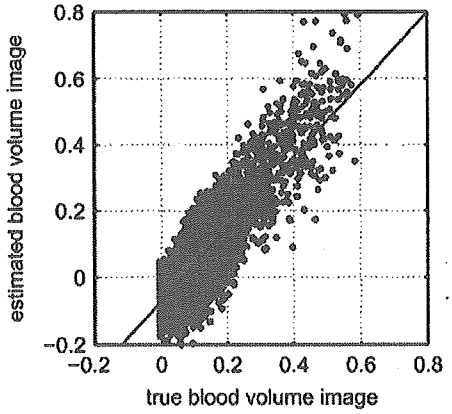

Fig. 6. Scatter plot of voxel values of the two blood volume images. The two images are the blood volume image estimated from the simulated FDG-PET images by EPICA, and the true blood volume image measured by PET using ^{15}O-CO inhalation, respectively ($y = 1.09x - 7.06 \times 10^{-2}; r = 0.83; n = 24\,974$).

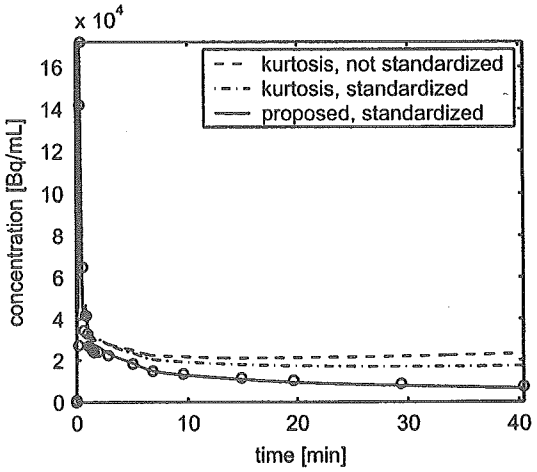

Fig. 7. The pTACs estimated: using kurtosis without standardization (dashed line), using kurtosis with standardization (dash-dot line), and using proposed objective function with standardization (solid line). The true pTAC values are plotted (open circles).

from the simulated images was performed under the following conditions: 1) using kurtosis-based FastICA without standardization; 2) using kurtosis-based FastICA with standardization,; 3) using EPICA (proposed objective function). The estimated pTACs are shown in Fig. 7. The deviation from the true pTAC values was large when objective function was kurtosis. There was little difference between the estimated blood volume images.

B. Human FDG-PET Studies

FDG-PET scans were performed on volunteers using a Headtome-V scanner (Shimadzu Co., Kyoto, Japan) in two-dimensional mode. The sensitivity, nonuniformity, and attenuation were corrected, and then the filtered-back projection was applied for image reconstruction using a low-pass filter with a full-width at half-maximum (FWHM) of 7 mm. The number of frames collected was 27 and the frame arrangements were 10 s × 6, 30 s × 3, 1 min × 5, 2.5 min × 5, and 5 min × 8. The frame intervals initially were set to be sufficiently short to estimate the pulse-like shape of the pTAC. Thirty slices were

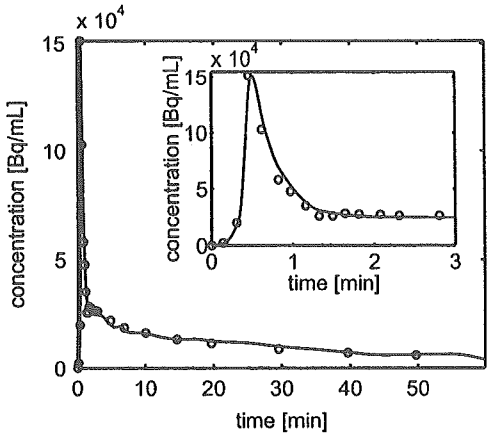

Fig. 8. Clinical result of the pTAC estimates. The pTAC-like estimate using EPICA (solid line) and the measured pTAC values (open circles). The estimated pTAC shape was scaled so that the peak value corresponded to the measured pTAC. A magnified view of the first section of data is shown in the inset. The parameters of the objective function in (6) were $\lambda = 50$ and $m = 0.3$. A total of 55 400 voxels were used to extract the pTAC.

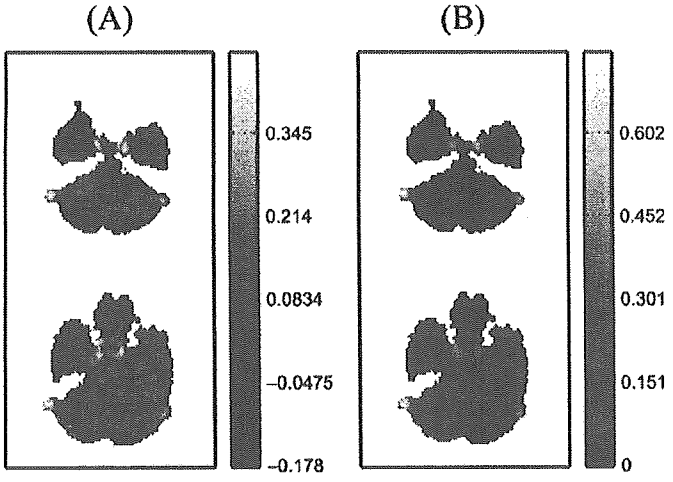

Fig. 9. (A) The blood volume image estimated from a human FDG-PET image sequence using EPICA, and (B) the blood volume image measured by PET using ^{15}O-CO inhalation. The parameters of the objective function in (6) were $\lambda = 50$ and $m = 0.3$.

acquired per scan, and each slice had 128 × 128 voxels. The 24 arterial blood samples were taken concurrently via an inserted catheter in the brachial artery. The blood volume image was also obtained using PET from ^{15}O-CO inhalation [12]. Extracranial voxels were manually masked before applying EPICA, and the time delay between the arterial plasma samples and the dynamic PET images was estimated from the averaged TAC over the whole brain using a nonlinear least squares estimation. Figs. 8 and 9 show the result of applying EPICA to human FDG-PET images. EPICA successfully extracted the pTAC from the FDG-PET images. The settings of the parameters (λ and m) in (6) did not affect the results of EPICA. The human FDG-PET data used $\lambda = 50$ and $m = 0.3$. The estimated blood volume image using EPICA included negative voxels. However, the spatial distribution of the estimated image was weakly correlated with the blood volume image measured by PET using ^{15}O-CO ($y = 0.69x + 3.1$) with a correlation coefficient of 0.76, suggesting that it is physiologically correct.

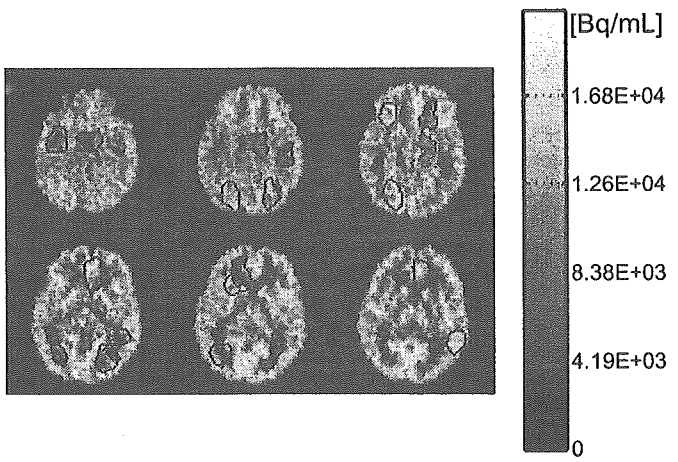

Fig. 10. Locations of ROIs. Twenty ROIs were placed on six slices.

To evaluate the estimated pTAC, 20 regions of interest (ROIs) were placed on six slices (slice numbers 11, 12, 13, 14, 15, and 16). The number of voxels per ROI was around 100 or 200. Fig. 10 shows the locations of the ROIs. The TACs were averaged over each ROI. The influx parameter [1] of the averaged TAC was estimated using the pTACs (the EPICA-estimated pTAC and that from the arterial plasma samples). It is defined as $K_i = K_1 k_3/(k_2 + k_3)$ and is proportional to the regional cerebral metabolic rate of glucose. The scale of the estimated pTAC was adjusted using the peak of the measured pTAC. As shown in Fig. 11, the influx parameters, K_i, were estimated using the EPICA-estimated pTAC and correlated well with those estimated using the exact clinical data. The correlation coefficient was 0.999, and the fitted line had almost unity slope ($y = 0.948x - 3.34 \times 10^{-4}$).

IV. Discussion

ICA is a statistical tool for the extraction of various useful information from biological data [15]. However, the following problems have been reported when applying ICA to real-world data.

Problem 1) The statistical properties of source signals are not always provided as *a priori* information.
Problem 2) The number of source signals is often unknown.
Problem 3) It is unlikely that source signals are independent of each other in a strict mathematical sense.

To address these three problems, three modifications were applied to measured dynamic PET images for the extraction of the pTAC.

The statistical properties of source signals in Problem 1 correspond to the features regarding the spatial distribution of the blood volume image and tissue image. These properties are considered to be dependent on the physiological or anatomical aspects of each subject, such that the characteristics of the two images are unknown in advance. In EPICA, enhancement locates voxel values of the tissue image near 1 or −1 and makes the blood volume image conform to a distribution with long tails. This allows us to use the converted distribution as *a priori* information. Therefore, the accuracy of the estimation did not vary greatly between subjects. The objective function can be

designed based on these known properties. The design of the objective function is also important in applying ICA to real-world data in order to estimate sources of interest. Some objective functions, such as kurtosis, Gaussian, and log cosh have been proposed [8]. These are general-purpose functions and are very useful in many situations. However, a specialized objective function in the extraction of the pTAC from the dynamic PET images is required because the general objective functions cannot estimate the pTAC correctly. Fig. 7 shows a comparison of the estimation under three conditions 1) using kurtosis without standardization; 2) using kurtosis with standardization; 3) using proposed objective function with standardization. The proposed function has the best performance, and standardization produced a very similar pTAC. The choice of parameters of the objective function for the actual data is an important and difficult decision. Fortunately, the results of EPICA only varied slightly for a range of the λ and m parameters [16].

As regards Problem 2, EPICA assumes that there are two source signals in the dynamic PET images, one is the blood volume image and the other is the tissue image. This is not strictly correct in the representation of a group of tTACs using single tTAC $c_t(t)$, because the shape of the tTAC varies with the kinetic parameters, (K_1, k_2, k_3). In ICA, if two columns of a mixing matrix are relatively similar, compared with other columns, the corresponding two components tend to be estimated as one component [17]. Differences between the shape of the tTACs are negligible compared with the difference between the pTAC and a group of tTACs. Therefore, dynamic PET images can be regarded as a linear combination of the pTAC and the representative tTAC.

Problem 3 means that the blood volume and the tissue images are not strictly independent. As a result of this dependence, the estimated blood volume images in Figs. 5 and 9 included negative voxels. Further investigation incorporating nonnegativity constraints in the EPICA algorithm is required. For example, ensemble learning for ICA [18] may be beneficial when estimating the two images having both independence and nonnegativity.

The EPICA approach was validated by computer simulation and clinical PET images using the PET blood volume measured quantitatively using ^{15}O-CO. There is good agreement between the estimated blood volume image and the true blood volume image, as shown in Fig. 6. Therefore, EPICA was very useful in extracting a pTAC that was similar to the true pTAC (Figs. 4 and 8). Furthermore, the influx parameter, K_i, estimated using the EPICA-estimated pTAC correlated well with that calculated from the arterial plasma samples. The estimated blood volume image had a high concentration region corresponding to a large sinus. EPICA does not depend on the kinds of tracers, and therefore this method has the potential to extract the pTAC from cerebral blood flow PET images if the scan intervals in the initial section, from zero to approximately 3 min, are arranged to be sufficiently short to capture the peak of the pTAC.

EPICA has an algorithm to distinguish the vessel-related information from the tissue-related information in dynamic PET images based on differences in their spatial distributions. This vessel-related information can have different meanings, such as activity histories in arteries and in veins. For PET kinetic studies, only the arterial history is essential. Fig. 11 underlines

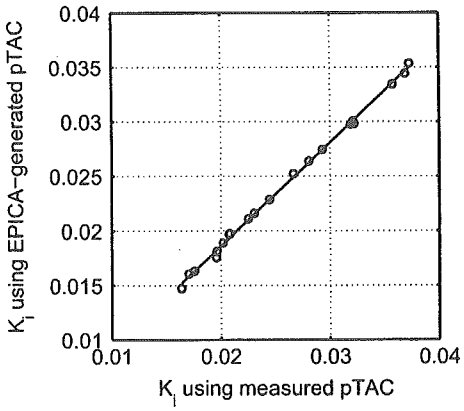

Fig. 11. Correlation of the influx parameters, K_i, estimated using the EPICA-estimated pTAC and the measured pTAC ($y = 0.948x - 3.34 \times 10^{-4}, r = 0.999, n = 20$). The K_i were estimated using 20 ROIs of the brain.

that the extracted vessel-related information originates exactly from the arteries because the physiological parameter, K_i, derived from arterial sampling, is highly correlated with the EPICA estimates.

The proposed method replaces arterial catheterization with arterial puncture. Arterial catheterization has some potential complications including infection, occlusion, bleeding, pseudoaneurysm, or thrombosis [19], [20]. In the case of patients suffering from thrombocytosis, a serious problem of digital gangrene and autoamputation of a left index finger after radial artery catheterization has been reported [21]. The risk is so small in PET that there were only two serious complications in 3 000 catheterizations of scans [20]. Because the risk increases with the duration of catheterization, the rate of temporary thrombosis was more than 20% after 5 h of catheterization, but the duration of a PET scan is less than 2 h. Although the risk is small, the protocol may increase the patient's risk, cost, and duration of the PET scan. Some previous trials were attempted to replace catheterization with puncture in some clinical measurements [22]–[24]. In the PET Center of TMIG, the average time for arterial catheterization is approximately 10 min. Sometimes, however, it takes more than 40 min to complete the arterial catheterization, in which case the PET measurement is aborted. Arterial puncture is much easier than catheterization, so a method like EPICA is valuable for PET scans as a routine procedure.

V. Conclusion

We have proposed a new method, extraction of the pTAC using ICA (EPICA), to extract the pTAC-related component from dynamic PET images without involving any serial arterial blood sampling, and have evaluated its validity using computer simulations and human FDG-PET studies. The proposed EPICA method is a modified version of ICA, taking into account real PET data. Negative images are used to achieve zero mean data and standardization emphasizes the differences between the two images. We conclude that EPICA shows promise for determining the pTAC in dynamic PET studies.

REFERENCES

[1] M. E. Phelps, S. C. Huang, E. J. Hoffman, C. Selin, L. Sokoloff, and D. E. Kuhl, "Tomographic measurement of local cerebral glucose metabolic rate in humans with (F-18)2-fluoro-2-deoxy-D-glucose: Validation of method," *Ann. Neurol.*, vol. 6, no. 5, pp. 371–388, 1979.

[2] S. C. Huang, M. E. Phelps, E. J. Hoffman, K. Sideris, C. J. Selin, and D. E. Kuhl, "Noninvasive determination of local cerebral metabolic rate of glucose in man," *Am. J. Physiol.*, vol. 238, no. 1, pp. E69–E82, 1980.

[3] H.-M. Wu, C. K. Hoh, Y. Choi, H. R. Schelbert, R. A. Hawkins, M. E. Phelps, and S.-C. Huang, "Factor analysis for extraction of blood time-activity curves in dynamic FDG-PET studies," *J. Nucl. Med.*, vol. 36, no. 9, pp. 1714–1722, 1995.

[4] J. S. Lee, D. S. Lee, J. Y. Ahn, G. J. Cheon, S.-K. Kim, J. S. Yeo, K. Seo, K. S. Park, J.-K. Chung, and M. C. Lee, "Blind separation of cardiac components and extraction of input function from $H_2^{15}O$ dynamic myocardial PET using independent component analysis," *J. Nucl. Med.*, vol. 42, no. 6, pp. 938–943, 2001.

[5] A. S. Houston, "The effect of apex-finding errors on factor images obtained from factor analysis and oblique transformation," *Phys. Med. Biol.*, vol. 29, no. 9, pp. 1109–1116, 1984.

[6] A. Hyvärinen and E. Oja, "A fast fixed-point algorithm for independent component analysis," *Neural. Comput.*, vol. 9, no. 7, pp. 1483–1492, 1997.

[7] J.-F. Cardoso, "Blind signal separation: Statistical principles," *Proc. IEEE*, vol. 86, no. 10, pp. 2009–2025, Oct. 1998.

[8] A. Hyvärinen, "Fast and robust fixed-point algorithms for independent component analysis," *IEEE Trans. Neural. Networks*, vol. 10, no. 3, pp. 626–634, May 1999.

[9] A. Hyvärinen, J. Karhunen, and E. Oja, "ICA by maximization of non-gaussianity," in *Independent Component Analysis*. New York: Wiley-Interscience, 2001, ch. 10, pp. 165–202.

[10] D. E. Kuhl, M. Reivich, A. Alavi, I. Nyary, and M. M. Staum, "Local cerebral blood volume determined by three-dimensional reconstruction of radionuclide scan data," *Circ. Res.*, vol. 36, no. 5, pp. 610–619, 1975.

[11] W. R. Martin, W. J. Powers, and M. E. Raichle, "Cerebral blood volume measured with inhaled $C^{15}O$ and positron emission tomography," *J. Cereb. Blood Flow Metab.*, vol. 7, no. 4, pp. 421–426, 1987.

[12] M. A. Mintun, M. E. Raichle, W. R. Martin, and P. Herscovitch, "Brain oxygen utilization measured with O-15 radiotracers and positron emission tomography," *J. Nucl. Med.*, vol. 25, no. 2, pp. 177–187, 1984.

[13] A. Stuart and J. K. Ord, *Kendall's Advanced Theory of Statistics*, 5th ed, London: C. Griffin, 1987, vol. 1.

[14] P. Comon, "Independent component analysis, a new concept?," *Signal Process.*, vol. 36, no. 3, pp. 287–314, 1994.

[15] M. J. McKeown, S. Makeig, G. G. Brown, T.-P. Jung, S. S. Kindermann, A. J. Bell, and T. J. Sejnowski, "Analysis of fMRI data by blind separation into independent spatial components," *Human Brain Mapp.*, vol. 6, no. 3, pp. 160–188, 1998.

[16] M. Naganawa, Y. Kimura, and A. Matani, "Modification of ICA for extracting blood vessel-related component in nuclear medicine: Contrast function and nonnegative constraints," in *Proc. ICA2003*, Nara, Japan, 2003, pp. 65–71.

[17] S. Makeig, T.-P. Jung, A. J. Bell, D. Ghahremani, and T. J. Sejnowski, "Blind separation of auditory event-related brain responses into independent components," *Proc. Nat. Acad. Sci.*, vol. 94, pp. 10 979–10 984, 1997.

[18] J. Miskin and D. J. C. MacKay, "Ensemble learning for blind image separation and deconvolution," in *Advances in Independent Component Analysis*. Berlin, Germany : Springer, 2000, ch. 7, pp. 123–141.

[19] R. F. Bedford and H. Wollman, "Complications of percutaneous radial-artery cannulation: An objective prospective study in man," *Anesthesiology*, vol. 38, no. 3, pp. 228–236, 1973.

[20] P. H. Jons, M. Ernst, J. Hankerson, K. Hardy, and A. J. Zametkin, "Follow-up of radial arterial catheterization for positron emission tomography studies," *Human Brain Mapp.*, vol. 5, pp. 119–123, 1997.

[21] K. H. Rehfeldt and M. S. Sanders, "Digital gangrene after radial artery catheterization in a patient with thrombocytosis," *Anesthesia Analgesia*, vol. 90, pp. 45–46, 2000.

[22] M. Frye, R. Dibenedetto, D. Lain, and K. Morgan, "Single arterial puncture vs arterial cannula for arterial gas analysis after exercise. Change in arterial oxygen tension over time," *Chest*, vol. 93, no. 2, pp. 294–298, 1988.

[23] J. Kissel, R. E. Port, J. Zaers, M. E. Bellemann, L. G. Strauss, U. Haberkorn, and G. Brix, "Noninvasive determination of the arterial input function of an anticancer drug from dynamic PET scans using the population approach," *Med. Phys.*, vol. 26, no. 4, pp. 609–615, 1999.

[24] J. Correia, "A bloody future for clinical PET?," *J. Nucl. Med.*, vol. 33, no. 4, pp. 620–622, 1992.

Mika Naganawa (M'01) was born in Gifu, Japan, in 1976. She graduated from the Graduate School of Frontier Sciences, University of Tokyo, Tokyo, Japan, and received the Ph.D. degree in science from the University of Tokyo in 2004.

She is now a Researcher with the Center Of Excellence program at the Graduate School of Information Processing, Nara Institute of Science and Technology, Nara, Japan. Her current interests are in the area of statistical signal processing.

Dr. Naganawa is a member of the Japanese Society of Nuclear Medicine and the Society of Instrument and Control Engineers.

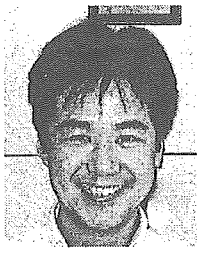

Yuichi Kimura (M'93) was born in Nishinomiya, Japan, in 1961. He received the Ph.D. degrees from Waseda University, Tokyo, Japan, in 1991 and from Tokyo Medical and Dental University from 2001.

He served as Assistant Professor of Waseda University from 1988 to 1991, and Nihon University from 1991 to 1994. Then, he was Assistant and then Associate Professor in Tokyo Medical and Dental University. From 1999, he is Senior Research Scientist at Positron Medical Center, Tokyo Metropolitan Institute of Gerontology. He is Chair of IEEE EMBS Japan Chapter since 2002. His major field is data and image analysis of PET image in clinical situation, and he is interested in an application of statistical approach to clinical images in nuclear medicine.

Dr. Kimura is a member of the Japanese Society for Medical and Biological Engineering, the Japanese Society of Nuclear Medicine, and other related societies. He received the awards from JSNM and JAMIT in 2000 and 1996.

Kenji Ishii was born in Tokyo, Japan, in 1959. He graduated from the Faculty of Medicine, Kyoto University, Kyoto, Japan, in 1985.

After he completed the training of clinical neurology, he started his research on clinical neuroscience with the technique of positron emission tomography at Positron Medical Center, Tokyo Metropolitan Institute of Gerontology in 1990. He is now head of the PET Clinic, Tokyo Metropolitan Institute of Gerontology, Tokyo, Japan. His main research interests are the physiology of brain aging and pathophysiological mechanism of aging related brain disorders such as Alzheimer's disease and Parkinson's disease. He is also interested in integrating the results from different modalities of neuroimaging techniques on the same platform to understand the brain function as a whole.

Keiichi Oda was born in Hokkaido, Japan, in 1957. He received the Ph.D. degree in engineering from the Science and Engineering, Waseda University, Tokyo, Japan, in 2003.

He is currently working as a researcher and his research activity concerns measurements and image processing of positron emission tomography (PET). He is also working as an operator of PET scanner as a radiological technologist.

He is a member of the Japanese Society of Nuclear Medicine, the Japanese Society of Radiological Technology, and the Japanese Society of Nuclear Medicine Technology. He received an award from the Japanese Society of Nuclear Medicine in 1997.

Kiichi Ishiwata was born in Kawasaki, Japan, in 1951. He received the Ph.D. degree in biochemistry from Tohoku University, Sendai, Japan, in 1979.

From 1981 to 1991, he served as Assistant Professor and then Associate Professor at the Cyclotron and radioisotope Center, Tohoku University. From 1991, he moved to the Positron Medical Center, Tokyo Metropolitan Institute of Gerontology as a senior research scientist. Presently he is a group leader of the PET group. His main research activity concerns development of radiopharmaceuticals used for positron emission tomography. He is the author of more than 200 scientific papers.

Dr. Ishiwata is a member of the Society of Nuclear Medicine, the Society of Radiopharmaceutical Chemistry and Biology, the Japanese Society of Nuclear Medicine and other Japanese learned societies.

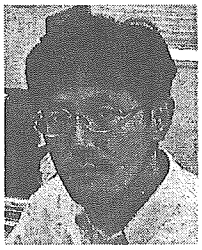

Ayumu Matani (M'96) received the B.S., the M.S., and the Ph.D. degrees from Osaka University, Osaka, Japan, in 1989, 1991, and 1998, respectively.

He was with Osaka Gas Co. Ltd, Japan (1991–1995), and with the Nara Institute of Science and Technology (NAIST), Nara, Japan, (1995–1998). He is now an associate professor in the Graduate School of Frontier Sciences, the University of Tokyo. His research interests include signal processing for complex biological systems.

J Neurosurg 103:414–423, 2005

Imaging of somatotopic representation of sensory cortex with intrinsic optical signals as guides for brain tumor surgery

TADASHI NARIAI, M.D., PH.D., KATSUSHIGE SATO, M.D., PH.D., KIMIYOSHI HIRAKAWA, M.D., PH.D., YOSHIHISA OHTA, M.D., YOJI TANAKA, M.D., KIICHI ISHIWATA, PH.D., KENJI ISHII, M.D., KOHTARO KAMINO, M.D., PH.D., AND KIKUO OHNO, M.D., PH.D.

Departments of Neurosurgery and Physiology, Tokyo Medical and Dental University; Positron Medical Center, Tokyo Metropolitan Institute of Gerontology, Tokyo, Japan

Object. Intrinsic optical signals in response to somatosensory stimuli were intraoperatively recorded during brain tumor surgery. In the present study, the authors report on the use of this technique as an intraoperative guide for the safe resection of tumors adjacent to or within the sensorimotor cortex.

Methods. In 14 patients with tumors adjacent to or within the sensorimotor cortex, intrinsic optical signals in response to somatosensory stimuli were recorded by illuminating the brain surface with Xe white light and imaging the reflected light passing through a bandpass filter (605 nm). Results were compared with intraoperative recordings of sensory evoked potentials in all 14 patients and with noninvasive mapping modalities such as magnetoencephalography and positron emission tomography in selected patients. In all but two patients, the somatosensory optical signals were recorded on the primary sensory cortex. Optical signals elicited by stimulation of the first and fifth digits and the three branches of the trigeminal nerve were recorded at different locations on the sensory strip. This somatotopic information was useful in determining the resection border in patients with glioma located in the sensorimotor cortex.

Conclusions. Optical imaging of intrinsic signals is a useful technique with superior spatial resolution for delineating the somatotopic representation of human primary sensory cortex. Furthermore, it can be used as an intraoperative monitoring tool to improve the safety and accuracy of resections of brain tumors adjacent to or within the sensorimotor cortex.

KEY WORDS • **intrinsic optical signal** • **somatosensory cortex** • **motor cortex** • **sensory evoked potential** • **optical imaging** • **magnetoencephalography** • **positron emission tomography** • **glioma**

OPTICAL imaging of intrinsic signals has proven to be useful in monitoring neural responses in the central nervous system in vivo.[6,12,13] Some investigators have successfully applied this technique in studies on the functional organization of visual[1,36,41] and somatosensory systems[9,20,39,44] in animal brains. Some research groups have applied this technique in human brains during neurosurgery.[3,4,14,26,28,35,40] We have established a system to monitor neuronal function of the human brain during brain tumor surgery and record the hierarchically distributed somatotopy in the primary somatosensory cortex and detailed finger sensory map.[33,34]

In the present report, we determined how the intraoperative optical imaging technique could be practically applied as a monitor of cortical neuronal function. Intrinsic optical signals in response to somatosensory stimuli were recorded while the patient was in a state of general anesthesia. We ascertained whether these signals corresponded with intraoperative cortical electrophysiological data and preoperative noninvasive brain mapping data obtained from MEG and PET studies. We also compared locations of the recording signals and the resection areas as well as postoperative symptoms to explore the potential of intraoperative optical imaging for determining resection borders of tumors located adjacent to the sensorimotor cortex without worsening neuronal function.

Abbreviations used in this paper: CBF = cerebral blood flow; ECD = equivalent current dipole; GBM = glioblastoma multiforme; MEG = magnetoencephalography; MET = ^{11}C methionine; MR = magnetic resonance; PET = positron emission tomography; SSEF = somatosensory evoked field; SSEP = somatosensory evoked potential; TN = trigeminal nerve; 3D = three-dimensional.

Clinical Material and Methods

Recordings were obtained in 14 patients with tumors adjacent to or within the sensorimotor cortex. Patient characteristics are described in Table 1. Optical recording was performed following cortical recording of SSEPs. Both sets of recordings were conducted while the patient was in a state of general anesthesia induced with isoflurane. Somatosensory stimuli were applied by electrically stimulating the median nerve and either the first and fifth digits or the first, second, and third branches of the TN. Stimuli consisted of 10 pulses delivered at 5 Hz for 2 seconds at a stimulation intensity of 10 mA, with an interstimulus interval of 20 seconds.

Optical Imaging

The method for optical imaging has been described in detail in a previous article.[33] Briefly, the recording site in the

TABLE 1

*Summary of characteristics in 14 patients with tumors adjacent to, or within, the sensorimotor cortex**

Case No.	Age (yrs), Sex	Diagnosis	Lesion Location	Stimulation Site	Validation Methods
1	52, M	meningioma	lt parietal (embedded in postcentral gyrus)	rt median nerve	MEG, CR
2	75, M	metastatic brain tumor	rt parietal	lt median nerve	CR
3	61, M	anaplastic oligodendroglioma	rt parietal (postcentral gyrus)	lt median nerve	MEG, CR
4	68, M	atypical meningioma	lt parasagittal sensorimotor area	rt median nerve	CR
5	57, M	anaplastic oligodendroglioma	rt parietal	lt 1st & 5th digits	CR
6	71, M	metastatic brain tumor	rt frontal (embedded in primary motor cortex)	lt 1st & 5th digits	MEG, CR
7	63, F	metastatic brain tumor	lt parietal	rt 1st & 5th digits	MEG, CR
8	44, M	metastatic brain tumor suspected (final diagnosis: brain abscess)	lt frontal (precentral gyrus)	rt 1st & 5th digits	MEG, CR
9	51, F	GBM	rt frontoparietotemporal (pre/postcentral gyrus)	lt V1&V3 nerves, lt median nerve	MEG, CR
10	49, M	oligodendroglioma	lt frontal (premotor cortex)	rt 1st & 5th digits	PET, fMRI, & CR
11	60, M	GBM	rt frontoparietal (pre/postcentral gyrus)	lt median nerve	CR
12	30, M	oligodendroglioma	lt parietal (postcentral gyrus)	rt V1, V2, & V3 nerves, rt 1st digit	fMRI, CR
13	38, F	oligodendroglioma	rt frontal (pre- & primary motor cortex)	lt 1st & 5th digits	fMRI, CR
14	69, F	metastatic brain tumor	rt frontal (premotor cortex)	lt 1st & 5th digits	fMRI, CR

* CR = cortical recording of SSEP; fMRI = functional MR imaging; V1, V2, V3 = 1st, 2nd, and 3rd branch of the TN.

cerebral cortex was stabilized with a glass plate. The cortical surface was illuminated using a Xe lamp driven by a stable direct current power supply through an operating microscope (Carl Zeiss, Inc., Thornwood, NY). The depth of focus of the operating microscope was set to approximately 500 μm under the cortical surface. Reflected light from the cortex passed through interference filters of different wavelengths. The filter used for displaying the surface of the cortex and its vascular pattern had a maximal transmission of 540 ± 30 nm, and the filter used for intrinsic imaging had a passband of 605 ± 5 nm (Asahi Spectra Co., Tokyo, Japan). We used this wavelength for two reasons. First, the wavelength coincides with the peak of the different spectra between the oxyhemoglobin and deoxyhemoglobin and maximizes the contribution of oximetry signals relative to other intrinsic signals.[2,11] Second, in previous animal experiments, we detected the largest intrinsic signal at the wavelength of 605 nm.[31,39,44]

Intrinsic optical imaging was performed using a differential video acquisition system (IMAGER 2001; Optical Imaging, Germantown, NY) through a charge-coupled device camera fitted to an operating microscope. One recording session consisted of eight blocks, each consisting of six or three stimulation trials and three nonstimulation (control) trials interlaced randomly, with an interval of 20 seconds between trials. During each trial, eight optical images were collected during 5 seconds and stored on a computer with data acquisition software (VDAQ; Optical Imaging). It took approximately 10 minutes to acquire images for each session. Optical reflectance images were represented by a fractional change (ΔR/R) to correct for uneven illumination by using a data-analyzing software program (TVMix; Optical Imaging). It usually took approximately 5 minutes to obtain a raw signal map, which was displayed on a monitor in the operation room. Although this rough image included noises and vasculature signal, it could be practically used as a guide to determine hand sensory area.

In a detailed analysis for scientific purposes and retrospective data comparisons, a color functional map was constructed as follows. We traced the optical response area by applying a modified version of the normalized threshold analysis[7,37] by using the data analysis programs TVMix and Transform (Fortner Research, LLC, Sterling, VA). With the software, we first located the local peak within the response area. We then calculated the median value of the signal amplitude within the no-response area. Normalization was conducted by subtracting from each image its median value and dividing the result by the amplitude of the local peak. To remove high-frequency noise, the ratio values were processed using a digital filter. Contour lines at 50% of the peak activation level were computed.

Cortical Recording of SSEPs

Intraoperative brain surface recording of SSEPs was performed in all patients. Recordings were obtained using a surface electrode consisting of four flat platinum discs aligned in a row, spaced at 1-cm intervals, and embedded in Silastic sheeting. The median nerve and the first or fifth digit on the side opposite the tumor were stimulated with a 10- to 20-mA current, and the evoked potential was recorded to define the central sulcus.[16]

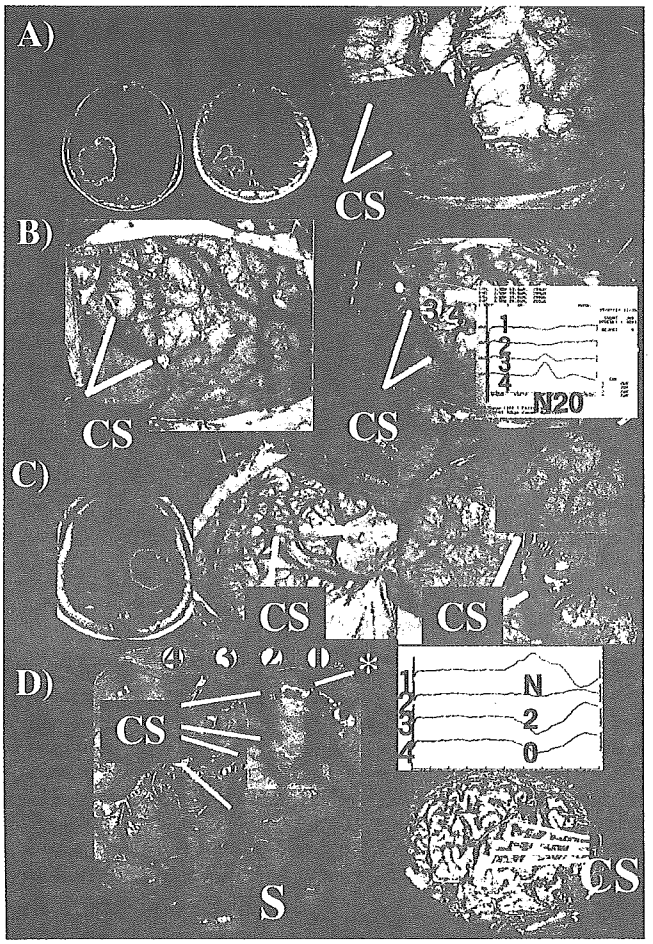

FIG. 1. Images for comparison between intraoperative SSEPs and optical signals. Case 11. A: In this patient with hemiplegia, neither the SSEP nor the optical signal was recorded. Case 3. B: As in nine other cases, the optical signal to somatosensory stimuli was recorded on the anterior edge of the postcentral gyrus together with the reversal of the N20 SSEP on the central sulcus. Case 8. C: An optical signal on the anterior edge of the postcentral gyrus was identified in a patient with massive ring-form enhancement (finally diagnosed as a brain abscess). The reversal of the N20 was recorded between electrodes 1 and 2 (findings were based on the operative record; SSEP waveform not available), which made it difficult to isolate the central sulcus. Case 12. D: The optical signal elicited by thumb stimulation was recorded in the postcentral gyrus *(left)* of a patient with a glioma in the face area (indicated in yellow in the *inset*). It was difficult to determine which of the two sulci (CS or S) was the true central sulcus in the SSEP recording. The true central sulcus determined with hand motor activation on functional MR imaging (marked in red in the *inset*) and morphological 3D brain surface imaging *(lower right)* was correctly indicated by optical imaging. CS = central sulcus; S = sylvian fissure.

Preoperative MEG and PET

Magnetoencephalography recording of SSEFs was performed in six patients before their surgeries by using a whole-head MEG system with 148-channel magnetometers (Magnes; Biomagnetic Technologies, San Diego, CA). On completion of the recording, the source current locations of the SSEFs in three dimensions and the ECD moments were calculated using a single-dipole model, assuming the brain to be a sphere. The ECDs that best explained the dominant source were determined using data recorded from a subset of channels.

The PET sensory mapping was compared with the optical imaging in one patient. A preoperative activation PET study was conducted together with tumor imaging, as described in a previous report.[23] The PET study was performed using a Headtome-V scanner (Shimadzu Corp., Kyoto, Japan). Transmission data were acquired with a rotating ^{68}Ge rod source for attenuation correction. An arterial catheter was inserted into the radial artery for blood sampling. Cerebral blood flow was measured during sensory tasks by using the PET-autoradiographic method with an intravenous bolus injection of 150 MBq $H_2{}^{15}O$ followed by data acquisition for 2 minutes. Electrical stimulation of the first digit was performed using the same device and protocol as those for intraoperative stimulation. The averaged control image was subtracted from the averaged task image to obtain the activation images.

The location of the ECD on MEG, the functioning area mapped using PET, and the tumor area delineated on MET-PET scanning (glioma) or Gd-enhanced MR imaging (other than glioma) were mapped on a 3D brain surface MR image. Image registration and 3D image processing were performed using image analysis software (Dr. View version 5.2; Asahi Kasei Informatics, Tokyo, Japan).

Results

Optical Signal and Cortical SSEPs

Intraoperative SSEPs were recorded in all patients by using surface electrodes to determine the location of the central sulcus. The brains of two patients (Cases 4 and 11) with hemiplegia revealed no detectable optical signal or SSEP in response to median nerve stimulation (Fig. 1A). The optical signal to somatosensory stimuli was recorded together with SSEP on the anterior edge of the postcentral gyrus in all 12 of the remaining patients (Fig. 1B).

In nine patients, optical imaging and SSEP provided similar mapping information on the location of the primary sensory cortex. In the other two patients (Cases 8 and 12), these two modalities provided discrepant information on the central sulcus. In the patient in Case 8 (Fig. 1C), who harbored a mass lesion (preoperatively diagnosed as a metastatic tumor but finally diagnosed as a brain abscess) in the motor and premotor areas, phase reversal of the N20 was detected where there was no cortical sulcus. The mass effect produced a markedly torturous central sulcus in this case. In the patient in Case 12 (Fig. 1D), who had a glioma in the face sensory area, phase reversal of the N20 was detected where there were two sulci. Somatosensory evoked potential recording was performed by exposing only a portion of the hand area in this case. The optical signal was detected at the anterior edge of the postcentral gyrus in both of these cases.

Somatotopic Representation of Optical Signal

Results of optical imaging and MEG were compared in six patients. The ECD was usually estimated not on the brain surface but deep in the sulcus. Given that the optical method is only valid for detecting signals on the brain surface, the locations of the ECD and optical signal were not

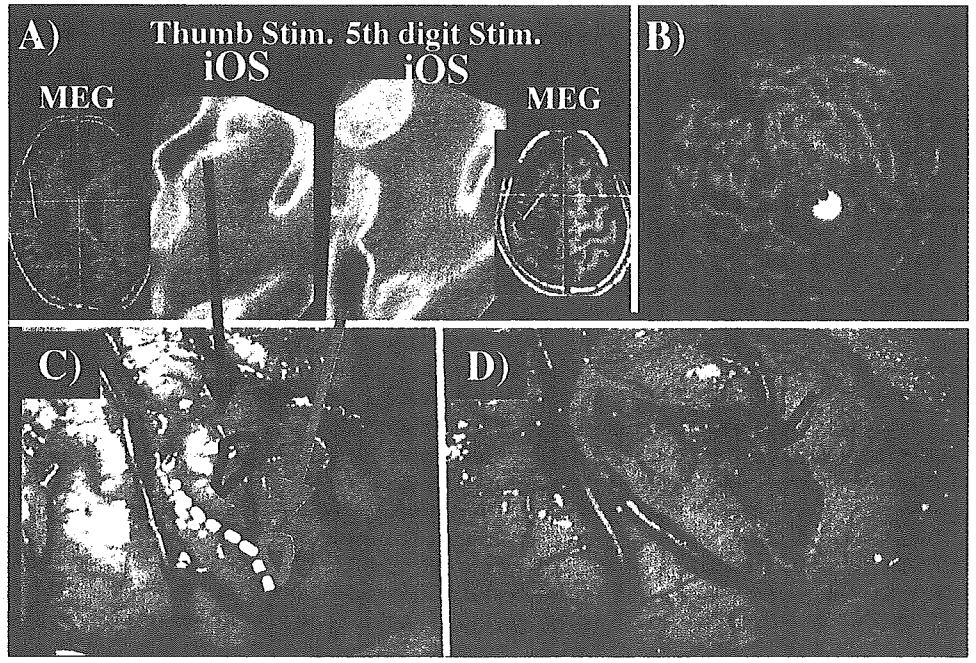

FIG. 2. Case 6. Images for comparison among MEG, optical signal, and intraoperative findings in a patient with a metastatic tumor in the precentral gyrus. A: In the MEG study, the ECD elicited by electrical stimulation of the thumb and fifth digit was estimated not on the brain surface but deep in the sulcus. Using the same stimulation, the intrinsic optical signals (iOS) were recorded on the surface of the postcentral gyrus. B: Once the ECD was projected onto the 3D brain surface image, the projected area corresponded with the location of the optical signal along the long axis of the central sulcus *(dotted line)*. C: The arachnoid membrane of the central sulcus was incised to approach a tumor embedded in the precentral gyrus. The incised portion was located between the areas where stimulation of the first and fifth digits elicited optical signals, as indicated by the *dotted line*. D: The posterior wall of the precentral gyrus in this portion protruded posteriorly, conforming with a landmark of the hand motor area, appearing as an inverse omega sign *(arrow)*. Stim. = stimulation.

identical. Nevertheless, once the ECD was projected onto the 3D brain surface image, the location of the optical signals corresponded with that of the ECD of cortical sensory responses against the median nerve and the first or the fifth digit on MEG along the axis of the central sulcus (Fig. 2).

We could not record trigeminal sensory responses on MEG because the stimulation site was covered by a whole-head detector system. Nevertheless, optical signals were detected at a location presumed from the morphological features and classic knowledge of somatotopy (homunculus) in the postcentral gyrus.[24]

In one patient (Case 6) with metastatic brain tumor and hand monoparesis on presentation, the arachnoid membrane of the central sulcus was opened to approach the tumor area. The opening site was located between areas where optical signals were elicited in response to stimulations of the first and fifth digits. The posterior wall of the precentral gyrus in this portion protruded posteriorly, conforming with a landmark of the hand motor area, appearing as an inverse omega sign.[45] Removal of a mass embedded in this protrusion led to a complete recovery of hand motor function (Fig. 2).

In a previous report, we analyzed the somatotopic representation of optical signals in relation to MEG results and discussed the neurophysiological significance.[33] We found that areas representing the digits were primarily different, but that the secondary response was recorded in the same location along the postcentral sulcus. Using this type of hierarchical organization, we could delineate the postcentral gyral portion representing the face and hand areas by recording optical signals, as was performed in Cases 9 and 12 (Figs. 3 and 4). This information was used to remove gliomas in the postcentral gyrus without causing any functional deficit in the hand.

Optical Signal and PET Scanning

We could compare the location of optical signals and CBF response (recorded on PET scanning) elicited by stimulation of the first and fifth digits in one patient (Fig. 5). To discuss the physiological significance, a PET activation image was made by depicting the difference in measured CBF between stimulated and resting conditions. In this patient, the most prominent CBF increase was observed not on the surface of the brain but along the postcentral gyrus facing the deep portion of the central sulcus. Note, however, that this CBF response was continuously traced to the edge of the postcentral gyrus, as was observed on the brain surface. The optical signal was located in exactly the same position as the cortical edge of the CBF response, which was situated at the anterior edge of the postcentral gyrus facing the central sulcus (Fig. 5).

Removal of Glioma Within the Sensorimotor Cortex While Monitoring Through Optical Imaging

Case 3. A nonenhanced lesion was identified in the right postcentral gyrus of this 61-year-old man presenting with

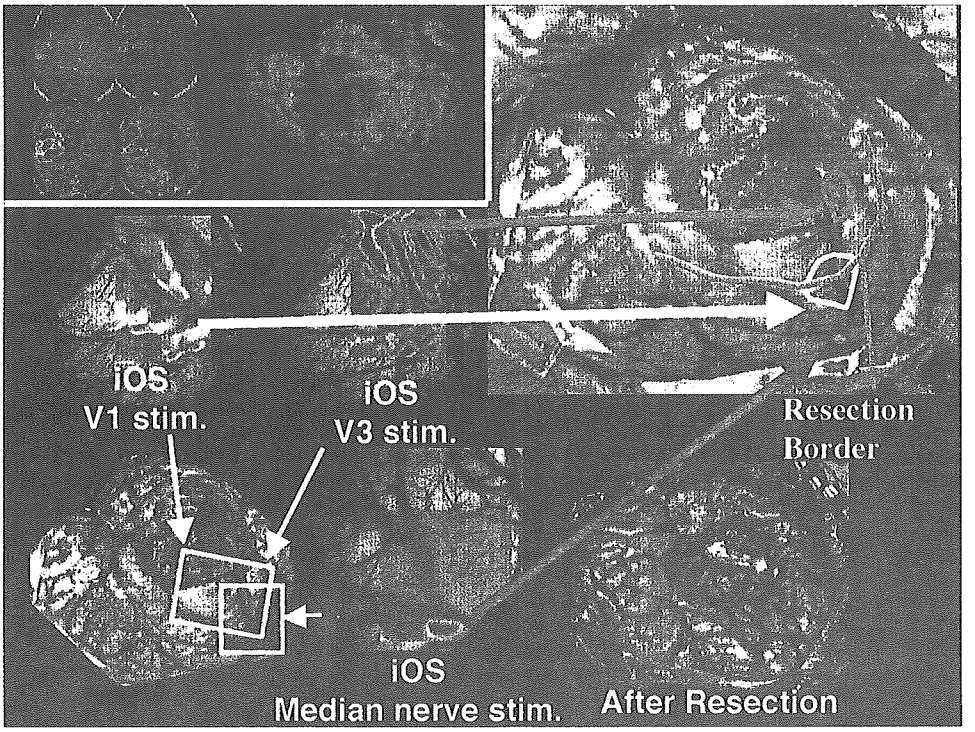

FIG. 3. Case 9. Images obtained in a patient with a GBM in the right face sensorimotor area. Preoperative MR images and MET-PET scans and their 3D reconstruction clearly delineated the location of the tumor *(upper left figures)* in relation to the functional organization of the brain. Intrinsic optical signals (iOS) elicited by stimulation of the median nerve and the first and third branches of the TN stimulation (V1 and V3) were obtained. The resected area included the postcentral gyrus where the optical signals from TN stimulation were recorded. The region where the signal from median nerve stimulation was recorded was protected. No permanent motor or sensory deficit occurred after the resection.

frequent partial epilepsy originating from the left brachial muscle and spreading to the arm and leg. The tumor area was delineated on an MET-PET image coregistered with an MR image. Three-dimensional expressions of the brain surface, tumor area, and location of the MEG dipole were used to plan a radical resection of the tumor. During the surgery, the optical signal in response to stimulation of the median nerve was recorded outside the tumor margin and the resection was performed without injuring the hand sensory area. The pathological diagnosis was anaplastic oligodendroglioma. Paresis of the left foot and severe left-sided spacial agnosia developed immediately after the operation, but both problems improved within 2 weeks. No hand motor deficit occurred during the entire treatment course. The patient returned home and resumed his vocation as a farmer (Fig. 6).

Case 9. A mass lesion was identified in the lower portion of the right frontoparietal lobe in this 51-year-old woman who presented with weakness in the left facial muscle and hand. The tumor area was delineated on an MET-PET scan coregistered with an MR image, and a 3D brain surface image indicated tumor involvement in the sensorimotor cortex for the face but not the hand. Intraoperative optical face and hand sensory stimuli confirmed that only the face sensory response was involved in the area with tumor infiltration. The resected area included the postcentral gyrus where TN stimulation had elicited an optical signal. The area where median nerve stimulation had elicited an optical signal was spared. A slight worsening of face and hand motor function occurred immediately after surgery—presumably because of postoperative edema—but the problem cleared up within 1 week. The tumor was histologically diagnosed as GBM, but the patient returned home without any deficit after the operation (Fig. 3).

Case 12. A calcified spot was pointed out in the left parietal cortex of this 30-year-old man presenting with generalized convulsions. An MR image demonstrated a small nonenhanced spot in the same area. A PET study revealed increased uptake of MET in and around the calcified area, indicating a glioma. Total resection was performed with the aid of a 3D brain surface image and intraoperative sensory monitoring with optical imaging. The resected tumor included the area where stimulation of the first and second branches of the TN elicited optical signals. The area where thumb stimulation elicited the optical signals was not injured. The effect of excision and postoperative edema caused intermittent dysphasia and weakness of the upper extremity, but these problems disappeared in 10 days. The patient returned to his occupation with no remaining symptoms (Fig. 4).

Discussion

Haglund and colleagues[14] were the first group to map successfully the function of the human brain by intrinsic optical imaging when they recorded stimulation-evoked epileptiform after-discharges and cognitively evoked functional activity. Several reports on the use of this method of mapping human brain function have followed.[3,4,26,40] We